A&A 461, 397–410 (2007)
DOI: 10.1051/0004-6361:20054493

Astronomy & Astrophysics

RASS-SDSS galaxy cluster survey⋆

V. The X-ray-underluminous Abell clusters

P. Popesso[1], A. Biviano[2], H. Böhringer[3], and M. Romaniello[1]

[1] European Southern Observatory, Karl Scharzschild Strasse 2, 85748, Germany
e-mail: ppopesso@eso.org
[2] INAF - Osservatorio Astronomico di Trieste, via G. B. Tiepolo 11, 34131, Trieste, Italy
[3] Max-Planck-Institut fur extraterrestrische Physik, 85748 Garching, Germany

Received 8 November 2005 / Accepted 26 May 2006

ABSTRACT

Aims. In this paper we consider a large sample of optically selected clusters, in order to elucidate the physical reasons for the existence of X-ray underluminous clusters.
Methods. For this purpose we analyzed the correlations of the X-ray and optical properties of a sample of 137 spectroscopically confirmed Abell clusters in the SDSS database. We searched for the X-ray counterpart of each cluster in the ROSAT All Sky Survey. We find that 40% of our clusters have a marginal X-ray detection or remain undetected in X-rays. These clusters appear too X-ray faint on average for their mass as determined by velocity dispersion; i.e. they do not follow the scaling relation between X-ray luminosity and virial mass traced by the other clusters. On the other hand, they do follow the general scaling relation between optical luminosity and virial mass. We refer to these clusters as the X-ray-underluminous Abell clusters (AXU clusters, for short) and designate as "normal" the X-ray detected Abell systems. We separately examined the distributions and properties of the galaxy populations of the normal and the AXU clusters.
Results. The AXU clusters are characterized by leptokurtic (more centrally concentrated than a Gaussian) velocity distribution of their member galaxies in the outskirts ($1.5 < r/r_{200} \leq 3.5$), as expected for the systems in accretion. In addition, the AXU clusters have a higher fraction of blue galaxies in the external region and show a marginally significant paucity of galaxies at the center. Our results seem to support the interpretation that the AXU clusters are systems in formation undergoing a phase of mass accretion. Their low X-ray luminosity should be due to the still accreting intracluster gas or to an ongoing merging process.

Key words. galaxies: clusters: general

1. Introduction

Clusters of galaxies are extremely important astrophysical tools for many reasons. They are the most massive gravitationally bound systems in the universe. Since they sample the high-mass end of the mass function of collapsed systems, they can be used to provide tight constraints on cosmological parameters such as Ω_m, σ_8, and Λ (Eke et al. 1996; Donahue & Voit 1999). Moreover, they are extremely powerful laboratories for studying galaxy formation and evolution. To investigate the global properties of the cosmological background, it is necessary to construct and study a large sample of clusters (Borgani & Guzzo 2001).

Several techniques exist for building cluster samples, each based on different cluster properties. The first attempts at a large, homogeneous survey for galaxy clusters was conducted by Abell (1958) with the visual identification of clusters on the Palomar Observatory Sky Survey (POSS) photographic plates. Similar catalogs were constructed by Zwicky and collaborators (Zwicky et al. 1968). Since then, a large number of optically selected samples have been constructed with automated methods: EDCC (Edimburgh Durham Cluster Catalog: Lumdsen et al. 1992), APM (Automatic Plate measuring; Dalton et al. 1994), PSCS (Palomar Distant Cluster Survey; Postman et al. 1996), EIS (ESO Imaging Cluster Survey; Olsen et al. 1999), ENACS (ESO Nearby Abell Cluster Survey, Katgert et al. 1996; Mazure et al. 1996), RCS (Red sequence Cluster Survey; Gladders & Yee 2000), and the samples derived from the Sloan Digital Sky Survey (Goto et al. 2002; Bahcall et al. 2003). The advantage of using optical data is that it is relatively easy to build large optically-selected cluster catalogs that allow one to investigate cluster properties with a statistically solid database. On the other hand, the main disadvantage of the optical selection is that the selection procedure can be seriously affected by projection effects. Only a very observationally expensive spectroscopic campaign can confirm the overdensities in 3 dimensions.

In 1978, the launch of the first X-ray imaging telescope, the *Einstein* observatory, began a new era of cluster discovery, as clusters proved to be luminous ($\geq 10^{42-45}$ erg s^{-1}), extended ($r \gtrsim 1$ Mpc) X-ray sources, which are readily identified in the X-ray sky. Therefore, X-ray observations of galaxy clusters provided an efficient and physically motivated method of identification of these structures. The X-ray selection is more robust against contamination along the line-of-sight than traditional optical methods, because the X-ray emission, unlike galaxy overdensities, is proportional to the square of the (gas) density. The ROSAT satellite, with its large field of view and better sensitivity, allowed a leap forward in X-ray cluster astronomy, producing large samples of both nearby and distant clusters (Castander et al. 1995; Ebeling et al. 1996a,b; Scharf et al. 1997; Ebeling et al. 2000; Böhringer et al. 2001, 2002; Gioia et al. 2001;

⋆ Appendix A is only available in electronic form at http://www.aanda.org

Rosati et al. 2002, and references therein). The disadvantage of X-ray cluster surveys is their lower efficiency and higher observational cost as compared to optical surveys.

It is clear that understanding the selection effects and the biases due to the different cluster selection techniques is crucial for interpreting the scientific results obtained from such different cluster samples. Castander et al. (1994) used ROSAT to observe cluster candidates in the redshift range 0.7−0.9 from the 3.5 square degree subsample of the Gunn et al. (1986) optical cluster catalog and found surprisingly weak X-ray emission. Bower et al. (1994) undertook ROSAT X-ray observations of optically selected clusters from the Couch et al. (1991) 46 deg^2 catalog. Bower et al. (1994) selected a random subset of the full catalog in the redshift range 0.15−0.66. The X-ray luminosity of almost all the selected clusters was found to be surprisingly low, suggesting, on the one hand, substantial evolution of the X-ray luminosity function between redshift $z = 0$ and $z \sim 0.4$ and, on the other, overestimated velocity dispersions for the nearby X-ray underluminous clusters, perhaps as a consequence of the contamination by galaxy filaments and of radial infall of field galaxies into the clusters. Similar results were obtained by Holden et al. (1997).

With the ROSAT Optical X-ray Survey (ROXS), Donahue et al. (2002) conclude that there is little overlap of the samples of X-ray-selected and optically-selected galaxy clusters. Only ∼20% of the optically selected clusters were found in X-rays, while ∼60% of the X-ray clusters were also identified in the optical sample. Furthermore, not all of the X-ray detected clusters had a prominent red-sequence, something that could introduce a selection bias in those cluster surveys based on color information (Goto et al. 2002; Gladders & Yee 2000). Ledlow et al. (2003) analyzed the X-ray properties of a sample of nearby bright Abell clusters, using the ROSAT All-Sky Survey (RASS). They find an X-ray detection rate of 83%. Gilbank et al. (2004) explored the biases due to optical and X-ray cluster selection techniques in the X-ray Dark Cluster Survey (XDCS). They find that a considerable fraction of the optically selected clusters do not have a clear X-ray counterpart, yet spectroscopic follow-up of a subsample of X-ray underluminous systems confirms their physical reality. Lubin et al. (2004) analyzed the X-ray properties of two optically selected clusters at $z \geq 0.7$ with XMM-Newton. They find that the two clusters are characterized by too small X-ray luminosities and temperatures, given their measured velocity dispersions. Similar results were obtained in the XMM-2dF Survey of Basilakos et al. (2004). They find many more optical cluster candidates than X-ray ones. Deeper XMM data confirmed that their X-ray undetected cluster candidates intrinsically have very low X-ray luminosities.

In this paper we consider a large sample of optically- and X-ray-selected clusters, in order to elucidate the physical reasons for the existence of underluminous optical/X-ray clusters. The starting point of this work was the analysis we conducted on a sample of X-ray selected clusters (Popesso et al. 2005a, Paper III of this series). Ninety percent of those systems were taken from the REFLEX and NORAS catalogs, which are X-ray flux-limited cluster catalogs entirely built upon the ROSAT-All-Sky Survey (RASS). The remaining 10% of that sample are groups or faint clusters with X-ray fluxes below the flux limits of REFLEX and NORAS. In Paper III we found an optical counterpart for each of the X-ray selected clusters of the RASS. Using optical data from the Sloan Digital Sky Survey (SDSS, see, e.g., Abazajian et al. 2003) for these clusters, we then studied the scatter of the correlations between several optical and X-ray cluster properties: X-ray and optical luminosities, mass, velocity dispersion, and temperature. In this paper we extend our analysis to a sample of *optically* selected clusters.

The paper is organized as follows. In Sect. 2 we describe the data and the sample of optically selected clusters used for the analysis. We also describe how we measure the optical luminosity, the velocity dispersion, the mass and the X-ray luminosity of the clusters. In Sect. 3 we analyze the correlation of both the X-ray and the optical cluster luminosities with their masses. In Sect. 4 we describe the optical properties of the Abell clusters without clear X-ray detection and compare them with those of normal X-ray emitting Abell systems. In Sect. 5 we discuss our results and give our conclusions.

We adopt a Hubble constant $H_0 = 70\ h$ km s^{-1} Mpc^{-1} and a flat geometry of the Universe, with $\Omega_m = 0.3$ and $\Omega_\Lambda = 0.7$ throughout this paper.

2. The data

The optical data used in this paper are taken from the SDSS (Fukugita et al. 1996; Gunn et al. 1998; Lupton et al. 1999; York et al. 2000; Hogg et al. 2001; Eisenstein et al. 2001; Smith et al. 2002; Strauss et al. 2002; Stoughton et al. 2002; Blanton et al. 2003; and Abazajian et al. 2003). The SDSS is still ongoing and consists of an imaging survey of π steradians of the northern sky in the five passbands u, g, r, i, z, covering the entire optical range. The imaging survey is being taken in drift-scan mode. The imaging data are being processed with a photometric pipeline specially written for the SDSS data (PHOTO, Lupton et al. 2001). For each cluster we defined a photometric galaxy catalog as described in Sect. 3 of Popesso et al. (2004, Paper I of this series, see also Yasuda et al. 2001). For the analysis in this paper we used only SDSS Model magnitudes.

The spectroscopic component of the survey is being carried out using two fiber-fed double spectrographs, covering the wavelength range 3800−9200 Å, over 4098 pixels. They have a resolution $\Delta\lambda/\lambda$ varying between 1850 and 2200, and together they are fed by 640 fibers, each with an entrance diameter of 3 arcsec.

The X-ray data were taken from the RASS. The RASS was conducted mainly during the first half year of the ROSAT mission in 1990 and 1991 (Trümper 1988). The ROSAT mirror system and the Position-Sensitive Proportional Counter (PSPC) operating in the soft X-ray regime (0.1−2.4 keV) provided optimal conditions for studying celestial objects with low surface brightness, in particular, due to the unlimited field of view of the RASS and the low background of the PSPC, this dataset is ideal for investigating the properties of nearby clusters of galaxies.

2.1. The cluster samples

2.1.1. The X-ray selected cluster sample

As reference X-ray cluster sample for the comparison between X-ray and optically selected clusters, we considered a subsample of the X-ray selected RASS-SDSS galaxy cluster sample of Popesso et al. (2005b, Paper II). The RASS-SDSS galaxy cluster catalog comprises 130 systems detected in the ROSAT All Sky Survey (RASS). The X-ray cluster properties and the redshifts were taken from different catalogs of X-ray selected clusters: the ROSAT-ESO flux limited X-ray cluster sample (REFLEX, Böhringer et al. 2001, 2002), the Northern ROSAT All-sky cluster sample (NORAS, Böhringer et al. 2000), the NORAS 2 cluster sample (Retzlaff 2001), the ASCA Cluster Catalog (ACC) from Horner et al. (2001), and the Group Sample (GS) of

Mulchaey et al. (2003). The subsample considered in this paper comprises the RASS-SDSS galaxy clusters with known mass (either the virial estimate from optical data or, when this is not available, the mass derived from the X-ray temperature) for a total number of 102 systems (69 clusters with known optical mass + 33 clusters with mass derived from the mass-temperature relation). The sample is drawn from the SDSS DR2 imaging data which cover 3324 square degrees. The considered cluster sample covers the entire range of masses and X-ray/optical luminosities, from very low-mass and X-ray/optical faint groups (10^{13} $M_{\odot}$) to very massive and X-ray/optical bright clusters (5×10^{15} $M_{\odot}$). The cluster sample comprises mainly nearby systems at the mean redshift of 0.1 and a few objects (10) in the range $0.25 \leq z \leq 0.37$. The redshift distribution of the cluster sample is shown in Fig. 1.

2.1.2. The optically selected cluster sample

The optically selected cluster sample considered in this paper is a subsample of the Abell cluster catalog (Abell 1958). We selected all the Abell clusters in the region covered by the 3rd data release (DR3) of the SDSS (5282 deg^{-2}). The Abell catalog is based on a visual inspection of galaxy overdensities. It is, therefore, affected by the presence of spurious detections due to projection effects. To exclude the spurious clusters from the catalog, we considered only the clusters with a spectroscopic confirmation of the galaxy overdensity. For this, we used the SDSS spectroscopic catalog, which provides spectra and redshifts for more than 250 000 galaxies with Petrosian magnitude $r_{\rm Petro} \leq 17.77$.

We estimated the mean cluster spectroscopic redshift $z_{\rm c}$ as the peak of the overdensity in the redshift distribution of the galaxies around the cluster coordinates. Since the purpose of this paper is to compare optical and X-ray properties of galaxy clusters, it is extremely important to avoid misclassification between the optical and the X-ray sources. Therefore, we checked our estimations of the mean cluster redshift with those available in the literature, as well as with the photometric $z_{\rm c}$ estimate obtained from the relation that links the mean redshift of a cluster with the apparent magnitude of its tenth brightest galaxy (Abell et al. 1989). Clusters for which discrepancies are found among the different $z_{\rm c}$ estimates were excluded from the final sample used in this paper.

Cluster members were selected among SDSS galaxies with available redshifts, as follows. First, we selected only galaxies within a circle of 2.15 Mpc radius (the Abell radius). We then grouped together those galaxies with intergalaxy velocity differences less than a critical value that depends on the total number of galaxies along the line-of-sight, according to the relation adopted by Adami et al. (1998a). This allowed us to define the cluster limits in velocity space. As an additional step, we applied the membership selection algorithm of Katgert et al. (2004) to *all* the galaxies (also outside an Abell radius) with velocities within the limits defined with the gapper procedure. This algorithm takes both the velocities and the clustercentric positions of the galaxies into account. The method is identical to that of den Hartog & Katgert (1996) where the cluster sample contains at least 45 galaxies, and it is a simplified version of it for smaller samples (for more details, see Appendix A in Katgert et al. 2004). It requires a cluster center to be defined. When possible, we adopted the X-ray center for this. However some clusters do not have secure X-ray detection, in which case the X-ray center cannot be accurately defined. In those cases we took the position of the brightest cluster member as the cluster center (see, e.g., Biviano et al. 1997). Analysis of clusters identified in cosmological numerical simulations indicates that the choice of the center is not critical for a correct performance of the membership selection algorithm (Biviano et al. 2006).

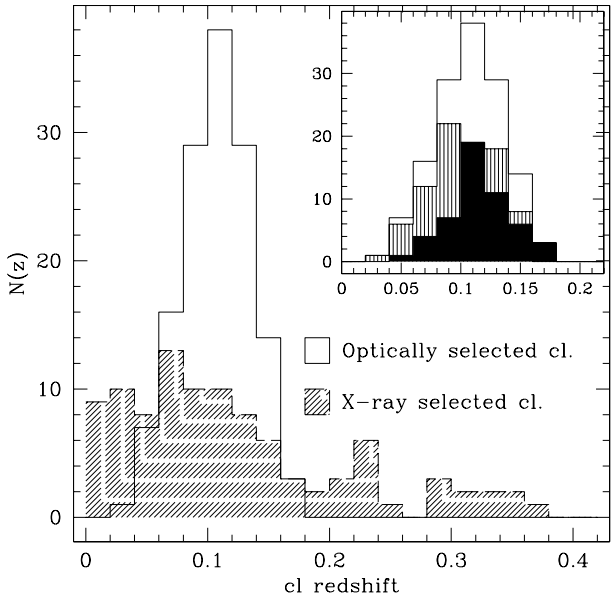

Fig. 1. Redshift distribution of the X-ray and optically selected cluster samples used in this paper. The solid line in the main panel shows the redshift distribution of the optically selected cluster sample, and the shaded histogram is the redshift distribution of the X-ray clusters. The small panel in the figure shows the redshift distribution of the X-ray detected (grey histogram) and the X-ray undetected (black histogram) optically selected clusters. The solid line in the small panel shows the redshift distribution of the whole optically selected cluster sample for comparison.

Only Abell clusters with at least 10 galaxy members were selected, since 10 is the minimum number of cluster members needed to calculate the cluster mass and velocity dispersion in a reasonable way (Girardi et al. 1993). Among the 280 Abell clusters in the region covered by DR3, 179 fulfil this requirement. Among these clusters, 38 are affected by problems of contamination, due to the presence of a close companion or a second system along the same line-of-sight but at different redshifts and 4 show large discrepancies between our estimate of $z_{\rm c}$ and the value derived from the literature or the $z_{\rm c} - m_{10}$ relation (Postman et al. 1985). Those systems were excluded from our final sample. Hence we were left with a sample of 138 Abell clusters, listed in the Appendix, along with their global properties. As shown in Fig. 1, the considered cluster sample comprises only nearby systems ($z < 0.25$) at the mean redshift of 0.1. As the X-ray reference sample, the optically selected cluster sample covers the entire range of masses and X-ray/optical luminosities, from the low-mass (faint X-ray/optical luminosity) regime (2×10^{13} $M_{\odot}$) to the high-mass (high X-ray/optical luminosity) regime (3×10^{15} $M_{\odot}$). We point out that the two cluster samples (X-ray and optically selected) considered in this work are not complete. However, for the purpose of this work we do not need complete cluster samples but clean X-ray and optically selected cluster samples spanning the whole cluster mass and luminosity range. The X-ray and optically selected cluster samples used in this work fulfill these requirements.

2.2. Optical luminosities

The estimate of the optical luminosity of a cluster, $L_{\rm op}$, requires subtraction of the foreground and background galaxy contamination. We considered two different approaches to the statistical subtraction of the galaxy background. We computed the local background number counts in an annulus around the cluster and global background number counts from the mean of the magnitude number counts determined in five different SDSS sky regions, each with an area of 30 deg^2. From our analysis we show the results obtained using the optical luminosity estimated with the second method, since the two methods produce only marginal differences in the $L_{\rm op}$ estimates. The cluster magnitude number counts in the virial region were obtained by subtracting from the galaxy counts measured within r_{200}, the local (global) field counts rescaled to the cluster area. The cluster magnitude number counts were converted in luminosity number counts after dereddening, K-correcting and transforming the apparent magnitudes in absolute magnitudes. The cluster optical luminosities were then obtained simply by summing up the luminosity number counts multiplied by the mean luminosity of the bin. The reader is referred to Paper I of this series for details of the comparison between optical luminosities obtained with different background subtraction methods and for the other technical details.

2.3. Velocity dispersions and virial masses

The virial analysis (see, e.g., Girardi et al. 1998) is performed on those clusters with at least 10 member galaxies. The velocity dispersion is computed on the cluster members, using the biweight estimator (Beers et al. 1990). The virial masses are corrected for the surface pressure term (The & White 1986) by adopting a profile of Navarro et al. (1996, 1997; NFW hereafter) with a concentration parameter, c, that depends on the initial estimate of the cluster virial mass itself. The c-mass relation is given by $c = 4 \times (M/M_{\rm KBM})^{-0.102}$ where the slope of the relation is taken from Dolag et al. (2004), and the normalization $M_{\rm KBM} \simeq 2 \times 10^{15}\ M_\odot$ from Katgert et al. (2004). The clusters in our sample span a range $c \simeq 3{-}6$.

The surface-pressure term correction requires knowledge of the r_{200} radius, for which we adopt the Carlberg et al. (1997) definition (see Eq. (8) in that paper) as a first guess. After the virial mass is corrected for the surface-pressure term, we refine our r_{200} estimate using the virial mass density itself. Let $M_{\rm vir}$ be the virial mass (corrected for the surface term) contained in a volume of radius equal to a chosen observational aperture, $r_{\rm ap}$, that we have set equal to the Abell radius, 2.15 Mpc. The radius r_{200} is then given by:

$$r_{200} \equiv r_{\rm ap}\,[\rho_{\rm vir}/(200\rho_{\rm c})]^{1/2.4} \qquad (1)$$

where $\rho_{\rm vir} \equiv 3M_{\rm vir}/(4\pi r_{\rm ap}^3)$ and $\rho_{\rm c}(z)$ is the critical density at redshift z in the adopted cosmology. The exponent in Eq. (1) is the one that describes the average cluster mass density profile near r_{200}, as estimated by Katgert et al. (2004) for an ensemble of 59 rich clusters.

For consistency the c-mass relation is used to interpolate (or, in a few cases, extrapolate) the virial mass $M_{\rm vir}$ from $r_{\rm ap}$ to r_{200}, yielding M_{200}. From M_{200} the final estimate of r_{200} is obtained, using the definition of M_{200} itself.

Even if the completeness level of the SDSS spectroscopic sample is very high, in the central regions of galaxy clusters such a level is likely to drop because fibers cannot be placed closer than 55 arcsec. We estimate that the spectroscopic completeness drops to ∼70% in the central ∼0.1 Mpc cluster regions. This affects the observed number-density profile of a cluster, and hence our virial mass estimates (see, e.g., Beers et al. 1984). Using the average cluster number-density profile, we estimate that this effect of incompleteness translates into an average over-estimate of the virial mass of only ∼5% (see Paper III of the series for more details about this estimate). Since the effect is very small, and much smaller than the observational uncertainties, we neglect this correcting factor in the following analysis.

2.4. X-ray luminosities

In order to create a homogeneous catalog of X-ray cluster properties, we searched for the X-ray counterparts of all the 137 Abell clusters, and compute their X-ray luminosity, $L_{\rm X}$, using only RASS data.

The X-ray luminosities are calculated with the growth curve analysis (GCA) method used for the NORAS and REFLEX cluster surveys (Böhringer et al. 2000) based on the RASS3 data base (Voges et al. 1999). The GCA method is optimized for the detection of the extended emission of clusters by assessing the plateau of the background subtracted cumulative count rate curve. We use as a final result the total flux inside the radius r_{200}, which is corrected for the missing flux estimated via the assumption of a standard β-model for the X-ray surface brightness (see Böhringer et al. 2000, for more details). The correction is typically only 8−10%, illustrating the high effectiveness of the GCA method for sampling the flux of extended sources.

We checked by eye all the X-ray sources associated to the Abell clusters. We found a secure X-ray detection for 86 systems out of the 137 isolated and well classified Abell clusters. Another 27 have a marginally significant detection (between 2 and 3σ), and another 24 do not have clear X-ray emission (detection level $\sim 1\sigma$ or no detection at all). The GCA method provides an estimate of the X-ray detection also in the case of dubious X-ray detection, but the percentage error is higher than 80%, and the estimate has to be considered as an upper limit. In 7 cases out of the 24 systems without X-ray detection, the GCA method failed completely to provide an estimate of $L_{\rm X}$. The X-ray luminosity ended up to be negative after the background subtraction. For those systems, the X-ray luminosity was set equal to zero. We discuss in detail the nature of these 27 + 24 clusters with marginal or no X-ray detection in the following sections. We refer to these 51 systems in the next paragraph as "clusters without secure X-ray detection".

3. X-ray versus optical properties

In this section we present the relations among the bolometric X-ray luminosity, the cluster mass, M_{200}, and the optical i-band luminosity, $L_{\rm op}$. The bolometric X-ray luminosity was derived by correcting the X-ray luminosity in the ROSAT energy band (0.1−2.4 keV) with the bolometric correction corresponding to the cluster temperature. The cluster temperature was estimated from the cluster mass using the $T_{\rm X} - M_{200}$ relation given in Paper III. We performed an orthogonal linear regression in logarithmic space for each of the analyzed relations. The orthogonal regression was performed with the software package ODRPACK (Akritas & Bershady 1996). Table 1 lists the values of the best fit parameters and the scatter for all the analyzed correlations. In the table, "X-ray" refers to the X-ray selected systems with known mass, taken from the RASS-SDSS galaxy cluster catalog (Paper III), "Abell" refers to the whole Abell sample considered in this work, and "A+X-ray" refers to the Abell sample

plus the X-ray selected cluster sample. "A($P_{\rm DS} > 0.1$)+X-ray" refers to the X-ray selected clusters plus the Abell sample without the clusters with unsecure X-ray detection and the systems with high level of subclustering. The table lists three estimations of the scatter for each relation: σ is the orthogonal scatter of the A-B relation (where $A = 10^{\beta} \times B^{\alpha}$), σ_A is the scatter in the A variable and σ_B is the scatter in the B variable. All the scatter values in the table are expressed in dex, while all the errors are given at the 95% confidence level.

3.1. The $M - L_{\rm X}$ relation and the Abell X-ray underluminous clusters

Panel a of Fig. 2 shows the $L_{\rm X} - M_{200}$ relation obtained from the X-ray selected RASS-SDSS galaxy cluster sample. The RASS-SDSS galaxy cluster sample comprises 102 systems. For 69 of them the mass, M_{200}, was calculated through the dynamical analysis as explained in Sect. 2.3. For the remaining 33 objects, the mass was calculated using the known ICM temperature in the M-T relation given in Paper III. The solid line in panel a of Fig. 2 shows the best-fit line obtained with the whole sample (102 clusters) and the dashed line shows the best fit line obtained using the 69 clusters for which the mass is calculated as for the Abell Clusters.

Panel b of Fig. 2 shows the location of the 86 Abell clusters with clear X-ray detection in RASS relative to the best fit obtained on the X-ray selected sample. Panel c shows the behavior of the Abell systems without secure X-ray detection in the RASS in the same diagram.

As shown by panel d of Fig. 2, the scatter of the $L_{\rm X} - M_{200}$ relation increases significantly when the Abell clusters are added to the sample of RASS-SDSS clusters. The best-fit parameters of the $L_{\rm X} - M_{200}$ relation obtained by considering the Abell and RASS-SDSS clusters together is consistent with the relation found for only the RASS-SDSS clusters (see Table 1). However, the orthogonal scatter increases from 44 to 65%. The RASS-SDSS clusters sample comprises several clusters (10 objects) at redshifts higher than the redshift range of the Abell clusters. Thus, to check the possible effect of evolution on the scatter of the considered relation, we perform the analysis by considering the RASS-SDSS clusters in the same redshift range as the Abell clusters. The resulting correlations are perfectly consistent with the results listed in Table 1 for all the considered cluster sample. The scatter increase is not only due to the Abell clusters without clear X-ray detection. Instead, a large contribution to the increase in the scatter is given by the normal Abell clusters, which show a high level of subclustering. In fact, the presence of substructures causes the cluster mass to be overestimated. Therefore the systems presenting subclustering should deviate from the relation. We quantify the presence of galaxy substructures in the whole Abell cluster sample through the Dressler & Shectman (1988) statistical test. This test looks for deviations in the local velocity mean and dispersion from the global values. Here we adopt the slightly modified version of the test introduced by Biviano et al. (2002). We call $P_{\rm DS}$ the probability that a cluster does *not* contain substructures according to the Dressler & Shectman test. We find that the fraction of clusters with a probability >0.90 ($P_{\rm DS} < 0.1$) of having significant substructure is somewhat low (20%) compared to the results of previous studies (e.g. Dressler & Shectman 1988; Biviano et al. 1997). This is not surprising. We remind the reader that the 137 Abell clusters in our sample were selected to be relatively isolated and free of major contaminations along the line-of-sight (see Sect. 2.1). As shown in Fig. 3 the cluster with values of $P_{\rm DS}$ lower than 0.1 have the largest negative residuals from the best fit line. When the clusters with a high level of subclustering (20% of the total), together with the Abell systems with unsecure X-ray detection, are excluded from the linear regression, the best-fit parameters and the scatter of the relation are consistent with the values found in the case of the RASS-SDSS cluster sample. Table 1 lists the results of this linear regression in the line corresponding to the A($P_{\rm DS} > 0.1$) + X-ray sample, which refers to the Abell clusters with $P_{\rm DS} > 0.1$ plus the RASS-SDSS systems.

In order to cahracterize the different behaviors of the normal Abell clusters and the Abell systems without secure X-ray detection, we analyzed the distribution of the residuals of the Abell clusters relatively to the RASS-SDSS $L_{\rm X} - M_{200}$ relation, along the $\log(L_{\rm X})$ axis. The residuals were defined as $\Delta \log(L_{\rm X}) = \log(L_{\rm X,m}) - \log(L_{\rm X,p})$, where $L_{\rm X,m}$ is the measured cluster X-ray luminosity and $L_{\rm X,p} = 0.0776\, M_{200}^{2.04}$ is the $L_{\rm X}$ predicted by the $L_{\rm X} - M_{200}$ relation (see Table 1). Hence, a negative value of the residual indicates that the cluster has a low X-ray luminosity for its mass.

Panel e of Fig. 2 shows the distribution of the residuals of the normal Abell clusters. The median of the distribution is at -0.3 ± 0.3, and it moves to -0.1 ± 0.3 when the clusters with a high level of subclustering are excluded. This confirms that those systems obey the same $L_{\rm X} - M_{200}$ relation as the RASS-SDSS clusters.

Panel f of Fig. 2 shows the same distribution for the Abell clusters without secure X-ray detection (except clusters with zero $L_{\rm X}$). The median of the distribution is at -0.9 ± 0.4, which indicates that those clusters are *not* on the same $L_{\rm X} - M_{200}$ relation. Seventy percent of those systems have an X-ray luminosity that is more than 3 times lower than what is expected at their mass, and 50% of them have $L_{\rm X}$ one order of magnitude lower than the expectation. Hence, the Abell clusters without secure X-ray detection appear to be clearly X-ray underluminous for their mass. What causes this effect? Are those systems real clusters? The poor significance of the X-ray detection of these systems would suggest that it is a question of spurious detections in the redshift distribution. That is, the observed 3D galaxy overdensity of those systems is not due to a unique massive cluster but to the superposition of two interacting small groups. In fact, in this case a double-peaked velocity distribution of the two systems could be misclassified as a unique Gaussian distribution with a large velocity dispersion. As a consequence, the low X-ray luminosity of the two groups would be associated to the mass of a spurious massive cluster. To check this possibility we performed several tests. A double-peaked velocity distribution misclassified as a Gaussian should appear as a platikurtic distribution (more flat-topped than a Gaussian). This effect can be quantified with the the robust scaled tail index (T.I. herafter, Beers et al. 1991). Values of the T.I. higher than unity indicate a leptokurtic distribution (i.e. more centrally peaked than a Gaussian), while values lower than unity indicate a platikurtic distribution. Values close to unity indicate consistency with a Gaussian distribution. First, we computed the T.I. values of the individual cluster velocity distributions for those clusters with unsecure X-ray detection with at least 10 member galaxies within r_{200}. Out of 51 systems, 37 fulfill this requirement. Three out of 37 have platikurtic distributions and one has a leptokurtic one, while all the remaining distributions are consistent with a Gaussian. The confidence level used in the test is 99%; therefore, less than 10% of the clusters are suspected of being spurious detections. We perform the same analysis on the normal Abell clusters finding the same percentage of platikurtic distributions.

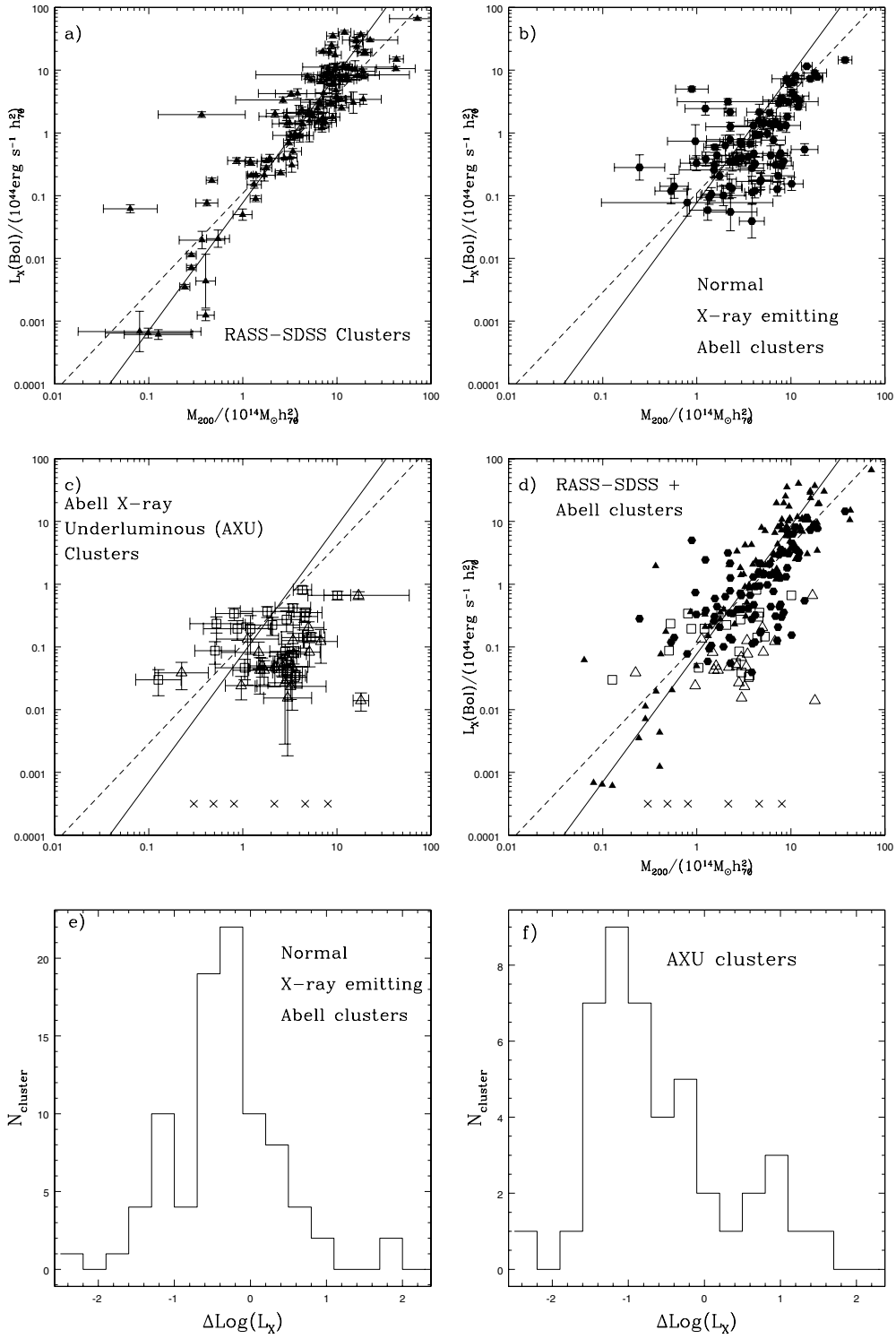

Fig. 2. $L_X - M_{200}$ relation. Panel **a)** shows the $L_X - M_{200}$ of the X-ray selected RASS-SDSS cluster sample (filled triangles). Panel **b)** shows the location of the Normal X-ray emitting Abell clusters (filled dots) relative to the best fit obtained in the X-ray selected sample. Panel **c)** shows the location of the AXU systems in the same diagram. The empty squares are the Abell clusters with marginally significant X-ray emission, and the empty triangles are the Abell clusters without X-ray emission (upper limits, see text for the explanation), the crosses are the Abell clusters for which the GCA method was not able to calculate the L_X upper limit (they are all plotted at $L_X = 10^{-40.5}$ erg s^{-1}). Panel **d)** shows the $L_X - M_{200}$ relation for the RASS-SDSS plus the whole Abell sample. The symbols in the panel have the same meaning as in the previous three panels. The solid line in the 4 panels is the best-fit line obtained in the whole X-ray selected sample of panel **a)** and the dashed line is the best fit obtained from the subsample of 69 RASS-SDSS clusters for which the mass was calculated as for the Abell clusters. Panel **e)** shows the distribution of the residuals of the normal X-ray emitting clusters. Panel **f)** shows the same distribution for the AXU clusters. The residuals are defined as $\Delta \log(L_X) = \log(L_{X,m}) - \log(L_{X,p})$, where $L_{X,m}$ is the measured cluster X-ray luminosity and $L_{X,p}$ the L_X predicted by the $L_X - M_{200}$ X-ray relation.

Table 1. The best fit parameters for the relations between several global cluster quantities, i.e. the bolometric X-ray luminosity, L_X(Bol), the virial mass, M_{200}, and the i-band optical luminosity L_{op}, for different samples of galaxy clusters.

A-B relation		sample					
A	B		α	β	σ	σ_B	σ_A
L_X(Bol)	M_{200}	X-ray	2.04 ± 0.08	–1.11 ± 0.06	0.16	0.21	0.43
		Abell	2.19 ± 0.14	–1.67 ± 0.14	0.23	0.32	0.48
		A+X-ray	2.12 ± 0.08	–1.32 ± 0.07	0.22	0.29	0.48
		A($P_{DS} > 0.1$)+X-ray	2.06 ± 0.08	–1.21 ± 0.06	0.18	0.23	0.46
L_X(Bol)	L_{op}	X-ray	1.72 ± 0.08	–0.98 ± 0.07	0.17	0.19	0.31
		Abell	2.01 ± 0.15	–1.17 ± 0.09	0.20	0.28	0.35
		A+X-ray	1.87 ± 0.08	–1.08 ± 0.06	0.19	0.25	0.35
L_{op}	M_{200}	X-ray	0.88 ± 0.03	–0.08 ± 0.02	0.13	0.18	0.16
		Abell	0.80 ± 0.07	–0.01 ± 0.04	0.14	0.21	0.22
		A+X-ray	0.83 ± 0.03	–0.05 ± 0.03	0.14	0.20	0.19

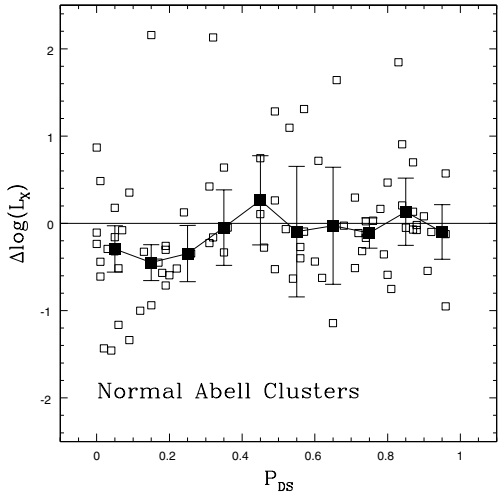

Fig. 3. The X-ray luminosity residuals $\Delta\log(L_X)$ from the best-fit $L_X - M_{200}$ relation of normal Abell clusters, vs. the Dressler & Shectman parameter P_{DS}. Systems with $P_{DS} < 0.1$ are considered to be characterized by subclustering. Filled squares with error bars represent the mean and dispersion of all points in bins of P_{DS}.

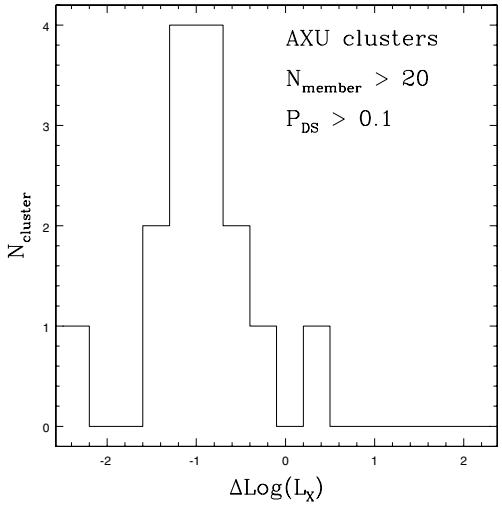

Fig. 4. Distribution of the residuals along the $\log(L_X)$ axis for the Abell clusters without secure X-ray detection with more than 20 spectroscopic members within 1 abell radius and with $P_{DS} > 0.1$. The residuals are defined as $\Delta\log(L_X) = \log(L_{X,m}) - \log(L_{X,p})$, where $L_{X,m}$ is the measured cluster X-ray luminosity and $L_{X,p}$ is the L_X predicted by the $L_X - M_{200}$ X-ray relation.

As a further test we used the Dressler & Shectman parameter to estimate the level of subclustering of those objects. Also this test is sensitive to the presence of different peaks in the redshift distribution and could reveal misclassifications. Only 5 clusters out of 51 systems without secure X-ray detection have values of P_{DS} lower than 0.1 (they comprise the 3 clusters with T.I lower than 1). Hence whether a cluster is detected or not in X-ray does not seem to be related to subclustering in the distribution of cluster galaxies.

An additional cause of uncertainties in the mass estimation is the use of a small number of spectroscopic members in the measurement. To check this point, we analyzed the residuals along the $\log(L_X)$ axis for the systems with a high number of members. Figure 4 shows the distribution of the residuals along the $\log(L_X)$ axis for the Abell clusters without secure X-ray detection with more than 20 spectroscopic members within 1 Abell radius and with $P_{DS} > 0.1$. The mass estimation of these clusters with a high number of member galaxies should be less affected by the systematics considered so far. That the distribution still peaks at -1.0 ± 0.3 confirms that these systems do not lie on the RASS-SDSS $M - L_X$ relations and that they are on average one order of magnitude fainter in the X-ray band than what is expected for their mass. Moreover, in Paper III of this series, we show that in the case of low level of subclustering, the masses obtained from the dynamical analysis of the cluster members are consistent with the hydrodynamical mass estimates.

On the basis of these analyses we conclude that the Abell clusters without secure X-ray detection are not spurious objects and that their difference with regard to the normal Abell systems and the RASS-SDSS clusters is physical. Due to their location relative to the X-ray $M - L_X$ relation, these objects are on average one order of magnitude fainter than what is expected for their mass. Their marginal detection or non-detection in X-rays suggests that RASS is too shallow to reveal the (probably weak) X-ray emission of these systems. Moreover, the detection depends on parameters that are not related to cluster properties like local RASS exposure, galactic N_H, and cluster distance. This conclusion is supported by the fact that several of these underluminous X-ray clusters are confirmed to be very faint X-ray systems by other independent analyses (Donahue et al. 2002; Ledlow et al. 2003), based on RASS PSPC-pointed observations with longer exposure times. For these reasons a better physical distinction between these systems and the normal Abell clusters is the underluminosity in X-rays of the cluster compared to the RASS-SDSS relation. However, since the errors on L_X for these clusters is so large our chosen subdivision is more

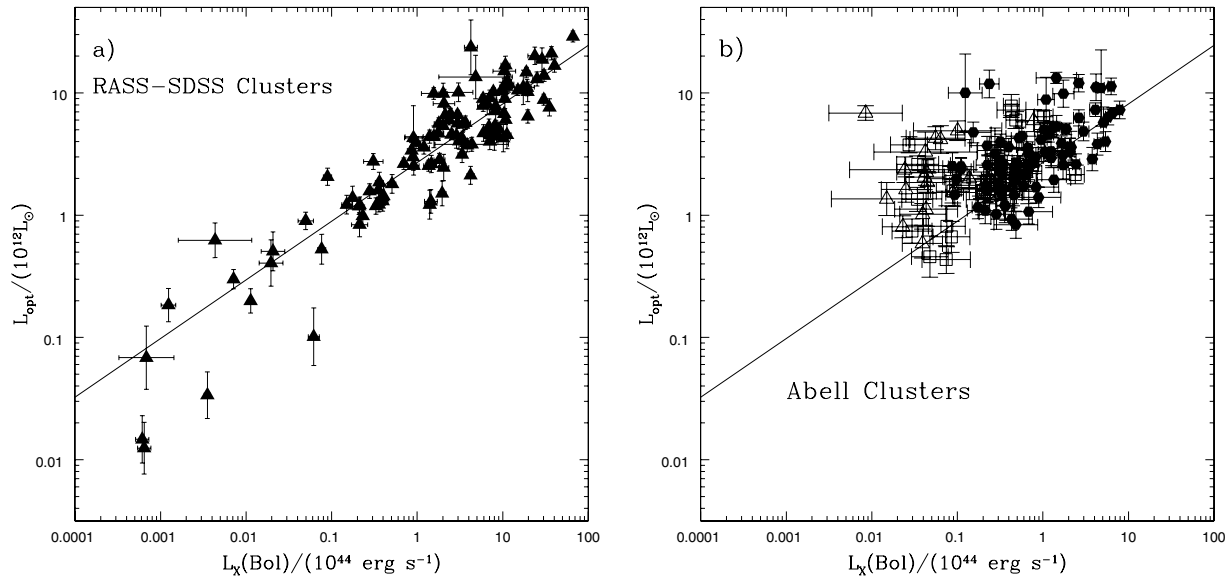

Fig. 5. $L_X - L_{op}$ relation. in panel **a)** the filled triangles are the X-ray selected clusters of the RASS-SDSS sample of Paper III. In panel **b)** the filled points are the normal X-ray emitting Abell clusters, the empty triangles are the AXU clusters with a marginally significant X-ray detection, the empty squares are the AXU clusters with no detection. The solid line is the best fit obtained from the RASS-SDSS clusters. The optical luminosity is computed in the *i*-band.

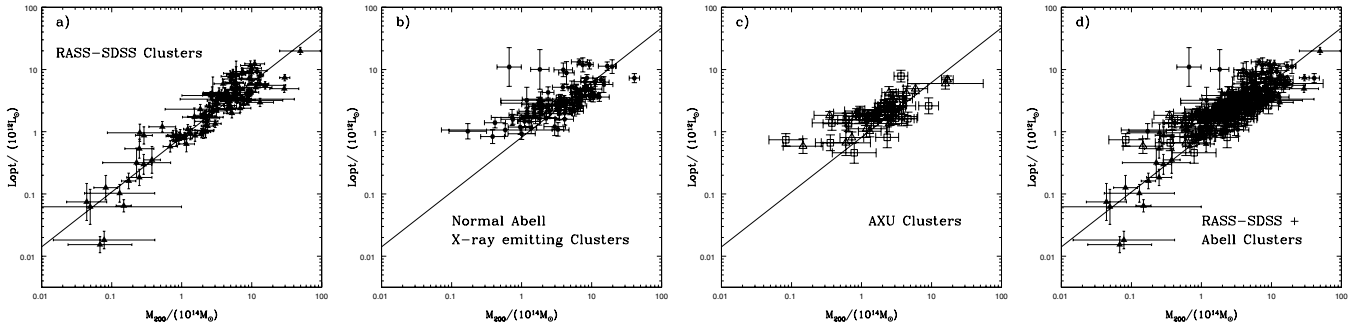

Fig. 6. $L_{op} - M_{200}$ relation. Panel **a)** shows the $L_{op} - M_{200}$ of the X-ray selected RASS-SDSS cluster sample (filled triangles). Panel **b)** shows the location of the normal X-ray emitting Abell clusters (filled dots) relatively to the best fit obtained in the X-ray selected sample. Panel **c)** shows the behavior of the AXU systems in the same relation. The empty squares are the AXU clusters with marginally significant X-ray emission, and the empty triangles are the totally underluminous AXU clusters. Panel **d)** shows the $L_{op} - M_{200}$ relation for the RASS-SDSS plus the whole Abell sample. Symbols in this panel have the same meaning as in the previous three panels. The solid line in all 4 panels is the best-fit line obtained in the X-ray-selected sample of panel **a)**. The optical luminosity was computed in the *i*-band.

practical. We call these objects X-ray underluminous Abell clusters (AXU clusters for short) throughout the paper.

3.2. The $L_X - L_{op}$ and the $L_{op} - M$ relations

Panel a of Fig. 5 shows the $L_X - L_{op}$ relation for the RASS-SDSS clusters (the optical luminosity is computed in the *i*-band). Panel b of the same figure shows the $L_X - L_{op}$ relation for the Abell sample. Similar to what was found for the $L_X - M_{200}$ relation, the best-fit regression lines obtained using the RASS-SDSS sample, or the combined RASS-SDSS and Abell samples, are not significantly different (see Table 1). Also in this case, the inclusion of the Abell clusters increases the scatter in the fitted relation. The AXU clusters are the main source of scatter, but the normal Abell clusters with high level of subclustering also contribute to increasing the scatter. The AXU clusters are significantly offset from the RASS-SDSS $L_X - L_{op}$ relation, while the normal Abell clusters are not. The mean residual of the normal Abell clusters along the $\log(L_{op})$ axis is 0.12 ± 0.25, while that of the AXU clusters is 0.54 ± 0.20. Thus, the AXU clusters are significantly underluminous in X-ray at a given optical luminosity compared to both the normal Abell clusters and the X-ray-selected RASS-SDSS systems.

Panel a of Fig. 6 shows the $L_{op} - M_{200}$ relation for the RASS-SDSS sample. Table 1 lists the best-fit parameters obtained performing a linear regression in the logarithmic space. Note that the slope of the relations and their scatter are not significantly different in other SDSS bands compared to the *i*-band. Panels b and c of Fig. 6 show the location of the normal Abell clusters and, respectively, of the AXU clusters, compared to the RASS-SDSS sample best-fit line. Clearly, both the normal Abell clusters and the AXU clusters obey the same $L_{op} - M_{200}$ relation as the X-ray selected clusters. The mean residual from the RASS-SDSS relation is ∼0 for both Abell cluster samples. Panel d of Fig. 6 shows that adding the Abell clusters to the sample of RASS-SDSS clusters does not alter the slope and the scatter of the relation (see also Table 1). The slope of the $L_{op} - M_{200}$ relation is confirmed to be less than 1. Therefore, we confirm the

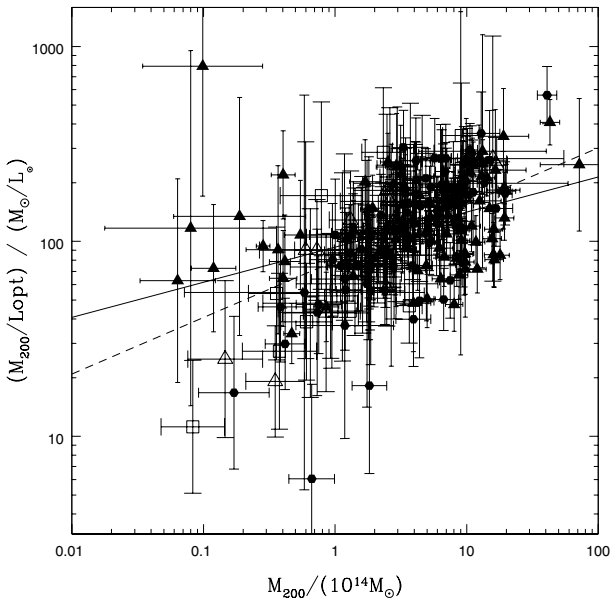

Fig. 7. The mass-to-light ratio versus the mass in the Sloan *i* band. The filled points are the normal Abell clusters, the empty triangles are the AXU clusters with a marginally significant X-ray detection, the empty squares are the AXU clusters without X-ray detection, the filled triangles are the X-ray-selected clusters of the RASS-SDSS galaxy cluster sample of Paper III. The solid line is the best fit obtained from the RASS-SDSS clusters, and the dashed line is the best fit obtained from the Abell plus the RASS-SDSS clusters.

result of Paper III that the cluster mass-to-light ratio M/L is an increasing function of the cluster mass, as shown in Fig. 7.

4. Nature of the AXU clusters

As shown in the previous section, the AXU clusters are not a source of scatter in the $L_{\rm op} - M_{200}$ relation; therefore, their optical luminosity does not differ from that of the normal X-ray emitting clusters of the same mass. On the other hand, they are significantly offset from the $L_{\rm X} - L_{\rm op}$ and $L_{\rm X} - M_{200}$ relations. In this section we try to elucidate the physical reason for this, in respect to whether the AXU clusters are different from normal X-ray emitting galaxy clusters. For this purpose, hereafter we compare the galaxy luminosity functions, the relative fractions of red and blue galaxies, galaxy number density profiles, and velocity distributions of both AXU and normal clusters. We also look for the presence of optical substructures, in order to see whether AXU clusters are more unrelaxed systems than normal clusters.

4.1. Luminosity functions

We used the SDSS photometric data to compute a composite galaxy luminosity function (LF) for the AXU systems by stacking the individual cluster LFs calculated within r_{200}. The individual LFs were obtained by subtracting the field number counts calculated within an annulus around the cluster, from the number counts in the cluster region, as described in Paper II. As in Popesso et al. (2006, Paper IV), we distinguished between early and late type galaxies using a color cut at $u - r = 2.22$, as suggested by Strateva et al. (2001). Figure 8 shows the composite LF of the AXU clusters for the whole (left-hand panel), the red (middle panel), and the blue (right-hand panel) cluster galaxy populations. For comparison we also plot the corresponding composite LFs of the normal Abell clusters, suitably renormalized to ease the comparison with the LFs of the AXU custers. The solid lines in the three panels of Fig. 8 are the best-fit double-Schechter (Schechter 1976) functions, obtained in Paper IV on the corresponding populations of the X-ray selected RASS-SDSS galaxy clusters. It is clear that there are no significant differences among the LFs of the three cluster samples, for any of the galaxy populations.

4.2. Blue galaxy fractions

In order to study the relative fraction of blue and red galaxies in the different cluster samples, we stacked the galaxy color distributions of all the clusters of each given sample together. Note that in this case we only considered spectroscopically confirmed cluster members, down to an absolute Petrosian magnitude $r_{\rm Petro} \leq -20$, and within $1.5\,r_{200}$. We find that there is no difference between the global color distributions of the normal Abell clusters and the AXU clusters. The AXU clusters do seem to have a larger fraction of blue galaxies than normal Abell clusters in the outer regions (see Fig. 9), but the statistical significance of this difference is marginal.

4.3. Galaxy number-density profiles

As in the analyses presented above, we computed the composite galaxy number-density profiles of the AXU clusters and the normal Abell clusters. These are shown in Fig. 10. In order to characterize these profiles, we fit two models to them. One is a King (1962) profile, $\Sigma(x) = \Sigma_0(1 + x^2)^{-1}$, where $x = r/r_{\rm c}$ and $r_{\rm c}$ is the core radius. The other model is the projected NFW profile, which in 3-dimensions reads $n(x) = n_0 x^{-1}(1 + x^2)^{-1}$, where $x = c_{\rm g} r/r_{200}$ and $c_{\rm g}$ is the concentration parameter. The surface density is then an integral of the 3D profile (see Bartelmann 1996, for more details).

For both the AXU and the normal Abell cluster samples, the composite radial profiles are better fit by a King profile (according to a standard χ^2 test). This agrees with previous results in the literature (Adami et al. 1998b; Díaz et al. 2005). The best-fit values of the core radii for the two samples of clusters are $r_{\rm c}/r_{200} = 0.209 \pm 0.006$ Mpc (normal Abell clusters) and $r_{\rm c}/r_{200} = 0.218 \pm 0.009$ Mpc (AXU clusters). Therefore the two profiles are perfectly consistent. However, we note that in the case of the AXU clusters an NFW profile also provides an acceptable fit to the data. This is, however, not due to a cuspier profile than that of the normal Abell clusters, but to the large error bar in the first bin of the number-density profile. Such a large error bar is due to a paucity of galaxies in the very center of AXU clusters. Hence AXU clusters, compared to normal Abell clusters, seem to have a lower central galaxy number-density. This is consistent with their larger fraction of blue galaxies (see the previous section) when we convolve this information with the morphology-density relation (Dressler 1980).

4.4. Galaxy velocity distributions

In this subsection we analyze the composite galaxy velocity distributions of the AXU clusters and the normal X-ray emitting clusters. The differences between the mean cluster velocity and the velocities of its member galaxies were normalized by $\sigma_{\rm c}$, the global cluster velocity dispersion. Each individual cluster velocity distribution was then normalized to the total number of cluster members in the region of the cluster being considered.

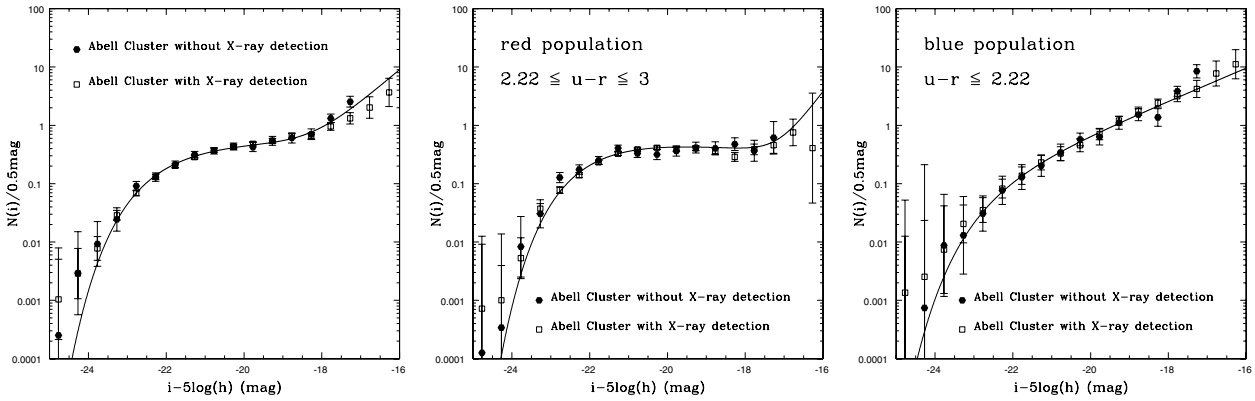

Fig. 8. The luminosity function of the normal Abell clusters and the AXU clusters. *Left panel*: composite cluster LFs of the whole galaxy population; filled dots, AXU clusters; open squares, normal Abell clusters; solid line, best-fit double Schechter LF obtained on the X-ray selected RASS-SDSS cluster sample (see Paper IV). *Middle panel*: same as left panel, but for the red galaxies only ($u - r \geq 2.22$). *Right panel*: same as left panel, but for the blue galaxies only ($u - r < 2.22$).

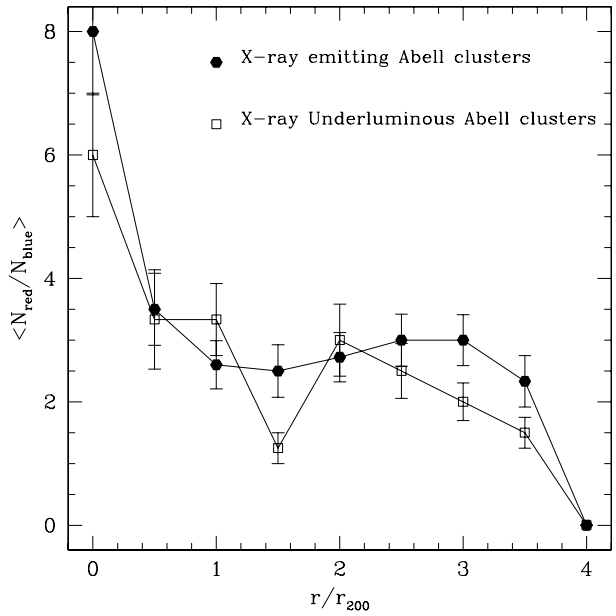

Fig. 9. The ratio of the numbers of red and blue cluster galaxies as a function of the clustercentric distance in units of r_{200}.

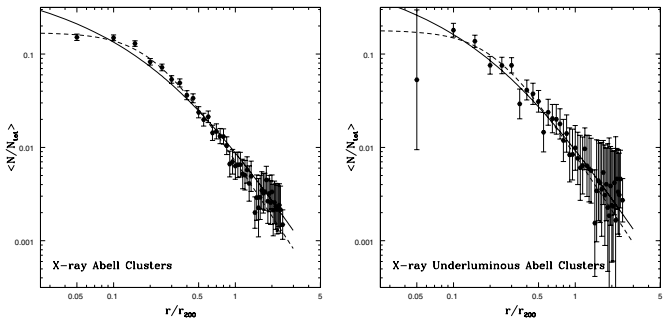

Fig. 10. The composite galaxy number density profiles of the normal Abell clusters (*left panel*) and of the AXU clusters (*right panel*). The solid and dashed lines are the best fits given by a projected NFW, and, respectively, a King density profile.

We considered only member galaxies with absolute Petrosian magnitude $r_{\rm Petro} \leq -20$ mag, which is brighter than the limiting magnitude of any cluster in our sample. We estimated the incompleteness of cluster spectroscopic samples by comparing the number of cluster spectroscopic members found within $3.5\,r_{200}$ and within the chosen absolute magnitude limit, with the number of cluster members obtained from the photometric data. The photometric sample is not affected by incompleteness down to the chosen magnitude limit. The number of photometric cluster members was obtained by subtracting the number of background galaxies at the same magnitude limit, rescaled by the cluster area, from the number of galaxies (cluster+field) in the cluster region. From this analysis we conclude that all the clusters have a spectroscopic completeness ≥80% down to $r_{\rm Petro} \leq -20$ mag.

Figure 11 shows the composite cluster velocity distributions of the normal Abell clusters and the AXU clusters, for two clustercentric distance intervals, $r/r_{200} \leq 1.5$ ("inner" sample hereafter) and $1.5 < r/r_{200} \leq 3.5$ ("outer" sample hereafter). The best-fit Gaussian dispersion decreases from 1.00 ± 0.01 to 0.96 ± 0.02 from the inner to the outer velocity distribution of the normal Abell clusters. The decrease is much stronger for the AXU clusters, from 1.00 ± 0.05 to 0.80 ± 0.07. Hence, the velocity dispersion profile is much steeper for the AXU clusters than for the normal Abell clusters. It is reminiscent of the steep velocity dispersion profile of late-type cluster galaxies (Biviano et al. 1997; Adami et al. 1998c; Biviano & Katgert 2004).

In order to gain more insight into the meaning of this result, we considered statistics that address the *shape* of the velocity distributions. A classical shape estimator, the kurtosis, is not recommended because it is very much influenced by the tails of the distribution. Instead, we consider the more robust T.I. The values of the T.I. for the considered distribution are 1.05, 0.88, 1.16, 1.45 for the four subsamples (inner normal, outer normal, inner AXU, outer AXU, respectively). As explained above, values higher than unity indicate a leptokurtic distribution (i.e. more centrally peaked than a Gaussian), while values lower than unity indicate a platikurtic distribution (i.e. more flat-topped than a Gaussian). Only the T.I. value 1.45 is significantly different from unity at >99% confidence level. We conclude that the outer velocity distribution of the AXU clusters is not only significantly narrower than all other velocity distributions, but it is also significantly non-Gaussian, leptokurtic in particular. Leptokurtic

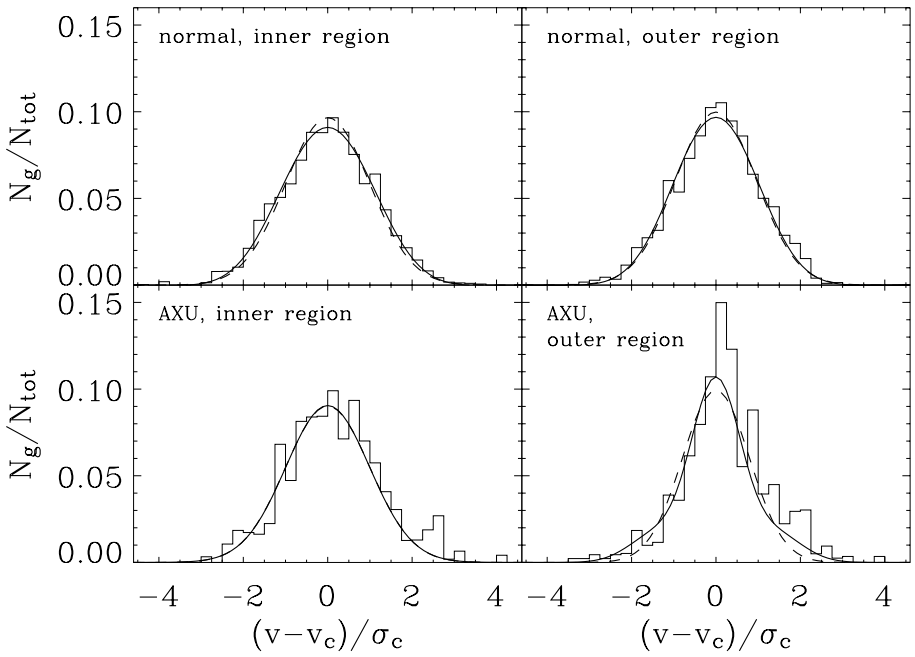

Fig. 11. The composite cluster velocity distributions. *Top-left panel*: the velocity distribution of galaxies in normal Abell clusters (histogram), within 1.5 r_{200}. *Top-right panel*: the velocity distribution of galaxies in normal Abell clusters (histogram), at clustercentric distances in the range 1.5−3.5 r_{200}. *Bottom-left panel*: the velocity distribution of galaxies in AXU clusters (histogram), within 1.5 r_{200}. *Bottom-right panel*: the velocity distribution of galaxies in AXU clusters (histogram), at clustercentric distances in the range 1.5–3.5 r_{200}. In each panel, the dashed line represents the best-fit Gaussian, and the solid line the best-fit obtained with a GH polynomial of order 4.

velocity distributions occur in the outer cluster regions when the external cluster members are characterized by radially elongated orbits (Merritt 1987; van der Marel et al. 2000). Cosmological simulations predict that haloes should display leptokurtic velocity distributions in their infall regions, characterized by ordered flows (Wojtak et al. 2005).

In order to estimate the amount of radial anisotropy required to fit the shape of the outer velocity distribution of AXU clusters, we determined the value of the Gauss-Hermite (GH hereafter) moment of order four (see, e.g., van der Marel et al. 2000). For completeness we determined the GH moments also for the velocity distributions of the other three subsamples. As expected from the T.I. analysis above, the GH polynomial fits to the velocity distributions of the normal Abell cluster galaxies and of the inner AXU cluster galaxies are very similar to the Gaussian fits, and only for the velocity distribution of the outer AXU cluster galaxies is there a clear difference between the GH polynomial fit and the Gaussian fit (see Fig. 11).

We then compared the values of the 4th-order GH moments of these velocity distributions with the predictions of the dynamical models of van der Marel et al. (2000, see their Fig. 8). While these predictions do depend on the number density distribution of the considered galaxy population, such a dependence is not strong. Hence, direct comparisons with van der Marel et al. dynamical models should provide useful information on the orbital anisotropy of the galaxy populations.

The 4th-order GH moments are −0.018 and −0.012 for the inner and outer velocity distributions of normal Abell cluster galaxies, respectively, and 0.002 and 0.106 for the inner and outer velocity distributions of AXU cluster galaxies, respectively. These values are all consistent with isotropic orbits, except that of the outer velocity distribution of the AXU cluster galaxies. For this population, we find $\sigma_r/\sigma_t \sim 2$, where σ_r and σ_t are the radial and tangential velocity dispersions of the galaxy population.

Analysis of the galaxy velocity distributions reveals a clear difference between normal Abell clusters and AXU clusters. The characteristics of the velocity distribution of AXU cluster galaxies is reminiscent of an infalling galaxy population, such as the one seen in numerical simulations in the external regions of dark matter haloes (Wojtak et al. 2005). The higher fraction of blue galaxies seen in AXU clusters, compared to that seen in normal Abell clusters, is certainly consistent with a higher fraction of infalling galaxies, since these must be part of the field galaxy population.

5. Discussion and conclusions

We have studied the X-ray and optical properties of 137 isolated Abell clusters. Each object has a confirmed 3D overdensity of galaxies. We looked for the X-ray counterpart of each system in the RASS data. Three classes of objects have been identified, where the classification is based on the quality of the X-ray detection. Eighty-six clusters out of the 137 Abell systems have a clear X-ray detection and are considered normal X-ray emitting clusters (the "normal Abell clusters"), 27 systems have a X-ray detection of low significance (less than 3σ), and 24 do not have clear X-ray detection (a rough estimate of L_X is provided but with huge statistical errors).

The normal Abell clusters follow the same scaling relations as observed in the X-ray-selected RASS-SDSS clusters. The 24 + 27 Abell clusters with unsecure X-ray detection appear to be outliers in the $L_X - M_{200}$ relation determined for X-ray luminous clusters. Their X-ray luminosity is on average one order of magnitude fainter than would be expected for their mass. A careful analysis of the 3D galaxy overdensity of these systems reveals that the individual galaxy velocity distributions in the virial region are Gaussian in 90% of the clusters and cannot be ascribed to the superposition of smaller interacting systems. We conclude that these Abell clusters with unsecure X-ray

detection in RASS are not spurious detections in the redshift distribution, but are a distinct class of objects. Due to their location with regard to the RASS-SDSS $M - L_X$ relation, we call them "Abell X-ray underluminous clusters", or AXU clusters for short. Several AXU clusters are confirmed to be very faint X-ray objects in the literature. Their X-ray flux is probably too low to be detected in the RASS survey, and yet, AXU clusters are not outliers from the $L_{\rm op} - M_{200}$ relation; i.e. they have a normal optical luminosity, given their mass. Hence, the distinctive signature of AXU clusters seems to lie in an X-ray luminosity that is unexpectedly low.

We looked for other properties of AXU clusters that make them different from normal Abell clusters. We have shown that AXU clusters do not have more substructures than normal Abell clusters. The galaxy luminosity functions within the virial region of the two cluster samples are very similar to each other. Also fairly similar are their galaxy number density profiles, even if the AXU clusters seem to lack galaxies near the core, relative to normal Abell clusters (but the significance of this result is low). The fractions of blue galaxies in the two kinds of clusters are only marginally different, since AXU clusters are characterized by a higher fraction.

The main difference between the two classes of objects lies in the velocity distribution of their member galaxies. The galaxy velocity distribution of the normal Abell clusters is perfectly fitted by a Gaussian both in the inner, virialized region ($\leq 1.5\, r_{200}$) and in the external region ($1.5\, r_{200} \leq r \leq 3.5\, r_{200}$). The AXU clusters instead only have a Gaussian velocity distribution within the virial region. In the external region, their velocity distribution is significantly more peaked than a Gaussian. The analysis of its shape by comparison with dynamical models available in the literature (van der Marel et al. 2000), suggests a radially anisotropic galaxy orbital distribution. However, the galaxies in this external region need not be in dynamical equilibrium with the cluster potential. As a matter of fact, a leptokurtic shape of the velocity distribution is a typical signature of the external, infall regions of dark matter haloes (Wojtak et al. 2005).

Analysis of the velocity distribution of the AXU clusters in their outer regions therefore suggests the presence of an unvirialized component of the galaxy population, still in the process of accretion onto the cluster. This infalling population would be mainly composed of field, hence blue, galaxies, which could then explain the excess of blue galaxies in AXU clusters, compared to normal Abell clusters. On the other hand, the Gaussian velocity distribution in the inner region suggests that there the galaxy population is dynamically more evolved, and probably virialized.

By a similar analysis of a different sample of X-ray underluminous clusters, Bower et al. (1997) proposed two different scenarios. AXU clusters could be severely affected by projection effects arising from surrounding large-scale structure filaments elongated along the line-of-sight. Their velocity dispersion, hence their virial masses would then be severely overestimated by interlopers in the filaments. In the alternative scenario, AXU clusters could be clusters that are not yet formed, or in the phase of forming, or, at least, caught at a particular stage of their evolution, while they are undergoing rapid mass growth.

Should the former of the two scenarios apply, we would expect AXU clusters to be X-ray underluminous for their mass, but they could still be optically luminous because we partly see the light of the filament projected onto the cluster. However, contamination by interlopers does affect the optical luminosity estimate, but not so much as the virial mass estimate and not so much in the i band, where contamination by the field (hence

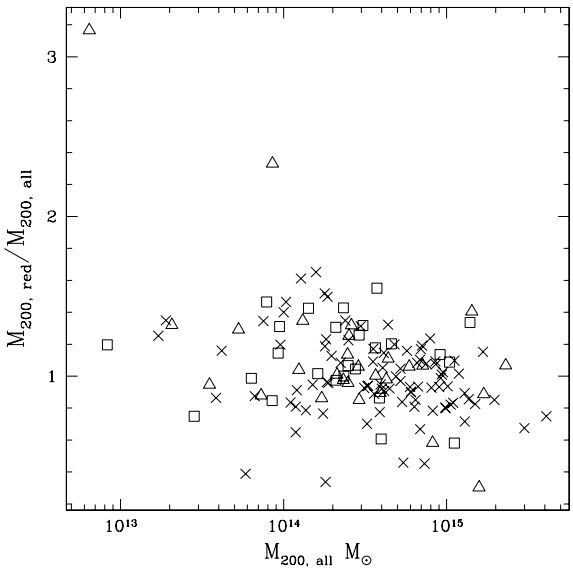

Fig. 12. Ratio of M_{200} calculated only with the red cluster members ($M_{200,\,\rm red}$) and M_{200} calculated with all the cluster members ($M_{200,\,\rm all}$) versus $M_{200,\,\rm all}$. The crosses are the "normal" Abell clusters, the empty triangles and squares are the AXU systems with marginally significant and without X-ray detection, respectively.

blue) galaxies should be small. Therefore, in such a scenario, it would be surprising that the clusters obey the $L_{\rm op} - M_{200}$ relation so well, which requires that the effects of the filament on the dynamical mass estimate and the optical light in the aperture both conspire not to produce an offset from the relation. It would also be surprising that the AXU clusters show a galaxy LF perfectly consistent with the steep LF found in galaxy clusters (see Papers II and IV) and not the flat LF observed in the field (Blanton et al. 2005). Instead, AXU clusters are not outliers from the $L_{\rm op} - M_{200}$ relation. If anything, AXU clusters are overluminous in the optical for their mass. In fact, the biweight-average (see Beers et al. 1990), i-band, mass-to-light ratios of normal Abell clusters and AXU clusters are $150 \pm 10\, M_\odot/L_\odot$ and $110 \pm 10\, M_\odot/L_\odot$, respectively.

As a further test, we have re-calculated the virial masses of all clusters by considering only red cluster members belonging to the red sequence in the $u - i$ vs. i color−magnitude diagram. In this way contamination by interlopers is strongly reduced (see, e.g., Biviano et al. 1997, 2006). Masses computed using all cluster members are compared to masses computed using only red-sequence members in Fig. 12. The cluster masses do not change significantly when only red-sequence members are used to calculate them, suggesting a low level of contamination by interlopers.

The results of our analyses therefore support the Bower et al. alternative scenario; namely, AXU clusters are systems in the stage of formation and/or of significant mass accretion. If AXU clusters are still forming, the intra-cluster gas itself may still be infalling or may not yet have reached the virial temperature. In addition, for AXU clusters undergoing massive accretion, it is to some degree possible that the continuous collisions of infalling groups is affecting the gas distribution, lowering its central density (such as in the case of the so-called "bullet cluster", see Barrena et al. 2002 and Clowe et al. 2004). In both cases the X-ray luminosity would be substantially lower than predicted for the virial mass of the system, because of its dependence on the square of the gas density. We note, however, that a virialized cluster undergoing a strong collision with an infalling group

would show up as a substructured cluster, yet the AXU clusters do not show an increased level of substructures when compared to normal Abell clusters. In summary, we know that the X-ray emission is very dominated by the central region, whereas the optical properties are more global. Therefore it could well be that we see a rough relaxation on the large scale (within $1.5r_{200}$) of the galaxy system reflected by a rough Gaussian galaxy velocity distribution, while the central region has not yet settled to reach the high density and temperatures of the luminous X-ray clusters.

In order to explore this further, we need much more detailed information on the distribution of the density and temperature of the intracluster gas in AXU clusters, something that cannot be done with the RASS data but that requires the spatial resolution and sensitivity of XMM-Newton.

Our results support the conclusion of Donahue et al. (2002) concerning the biases inherent in the selection of galaxy clusters in different wavebands. Although the optical selection is prone to substantial projection effects, the X-ray selection is also not perfect or not simple to characterize. The existence of X-ray underluminous clusters, even with large masses, makes it difficult to reach the needed completeness in mass for cosmological studies. Moreover, as discussed in Paper III, the relation between the X-ray luminosity and mass is not very tight even for the X-ray bright clusters, and the relation between cluster masses and optical luminosities is as tight or perhaps even tighter. Clearly, a multi-waveband approach is needed for optimizing the completeness and reliability of cluster samples.

On the other hand, it becomes clear that, for precision cosmology, we also need a more observationally oriented prescription for cluster selection from theory, rather than a mere counting of "relaxed" dark-matter haloes. Predicted distribution functions closer to the observational parameters, like temperature or velocity dispersion distribution functions and their relations to X-ray and optical luminosity, are needed.

Acknowledgements. We thank the referee F. Castander for the useful comments that helped in improving the paper. We thank Alain Mazure for useful discussions. Funding for the creation and distribution of the SDSS Archive has been provided by the Alfred P. Sloan Foundation, the Participating Institutions, the National Aeronautics and Space Administration, the National Science Foundation, the US Department of Energy, the Japanese Monbukagakusho, and the Max Planck Society. The SDSS Web site is `http://www.sdss.org/`. The SDSS is managed by the Astrophysical Research Consortium (ARC) for the Participating Institutions. The Participating Institutions are The University of Chicago, Fermilab, the Institute for Advanced Study, the Japan Participation Group, The Johns Hopkins University, Los Alamos National Laboratory, the Max-Planck-Institute for Astronomy (MPIA), the Max-Planck-Institute for Astrophysics (MPA), New Mexico State University, University of Pittsburgh, Princeton University, the United States Naval Observatory, and the University of Washington.

References

Abell, G. O. 1958, ApJ, 3, 211
Abell, G. O., Corwin, H. G. Jr., & Olowin, R. P. 1989, ApJ, 70, 1
Abazajian, K., Adelman, J., Agueros, M., et al. 2003, AJ, 126, 2081 (Data Release One)
Adami, C., Mazure, A., Biviano, A., Katgert, P., & Rhee, G. 1998a, A&A, 331, 493
Adami, C., Mazure, A., Katgert, P., & Biviano, A. 1998b, A&A, 336, 63
Adami, C., Biviano, A., & Mazure, A. 1998c, A&A, 331, 439
Akritas, M. G., & Bershady, M. A. 1996, ApJ, 470, 706
Bahcall, N. A., McKay, T. A,, Annis, J., et al. 2003, ApJ, 148, 243
Barrena, R., Biviano, A., Ramella, M., Falco, E. E., & Seitz, S. 2002, A&A, 386, 816
Bartelmann, M. 1996, A&A, 313, 697
Basilakos, S., Plionis, M., Georgakakis, A., & Georgantopoulos, I. 2004, MNRAS, 351, 989
Beers, T. C., Geller, M. J., Huchra, J. P., Latham, D. W., & Davis, R. J. 1984, ApJ, 283, 33
Beers, T. C., Flynn, K., & Gebhardt 1990, AJ, 100, 32
Beers, T. C., Forman, W., Huchra, J. P., Jones, C., & Gebhardt, K. 1991, AJ, 102, 1581
Biviano, A., & Katgert, P. 2004, A&A, 424, 779
Biviano, A., Katgert, P., Mazure, A., et al. 1997, A&A, 321, 84
Biviano, A., Katgert, P., Thomas, T., & Adami, C. 2002, A&A, 387, 8
Biviano, A., Murante, G., Borgani, S., et al. 2006, A&A, 456, 23
Blanton, M. R., Lupton, R. H., Maley, F. M., et al. 2003, AJ, 125, 2276
Blanton, M. R., Lupton, R. H., Schlegel, D. J., et al. 2005, ApJ, 631, 208
Böhringer, H., Voges, W., Huchra, J. P., et al. 2000, ApJS, 129, 435
Böhringer, H., Schuecker, P., Guzzo, L., et al. 2001, A&A, 369, 826
Böhringer, H., Collins, C. A., Guzzo, L., et al. 2002, ApJ, 566, 93
Borgani, S., & Guzzo, L. 2001, Nature, 409, 39
Bower, R. G., Bohringer, H., Briel, U. G., et al. 1994, MNRAS, 268, 345
Bower, R. G., Castander, F. J., Ellis, R. S., et al. 1997, MNRAS, 291, 353
Carlberg, R. G., Yee, H. K., & Ellingson, E. 1997, ApJ, 478, 462
Castander, F. J., Ellis, R. S., Frenk, C. S., Dressler, A., & Gunn, J. E. 1994, ApJ, 424, 79
Castander, F. J., Bower, R. G., & Ellis, R. S. 1995, Nature, 377, 39
Clowe, D., De Lucia, G., & King, L. 2004, MNRAS, 350, 1038
Couch, W. J., Ellis, R. S., MacLaren, I., & Malin, D. F. 1991, MNRAS, 249, 606
Dalton, G. B., Efstathiou, G., Maddox, S. J., & Sutherland, W. J. 1994, MNRAS, 269, 151
den Hartog, R., & Katgert, P. 1996, MNRAS, 279, 349
Díaz, E., Zandivarez, A., Merchán, M. E., & Muriel, H. 2005, ApJ, 629, 158
Dolag, K., Bartelmann, M., Perrotta, F., et al. 2004, A&A, 416, 853
Donahue, M., & Voit, M. 1999, ApJ, 523, 137
Donahue, M., Scharf, C. A., Mack, J., et al. 2002, ApJ, 569, 689
Dressler, A. 1980, ApJ, 236, 351
Dressler, A., & Shectman, S. A. 1988, AJ, 95, 985
Ebeling, H., Voges, W., Bohringer, H., et al. 1996a, MNRAS, 281, 799
Ebeling, H., Voges, W., Bohringer, H., et al. 1996b, MNRAS, 283, 1103
Ebeling, H., Edge, A. C., Allen, S. W., et al. 2000, MNRAS, 318, 333
Eisenstein, D. J., Annis, J., Gunn, J. E., et al. 2001, AJ, 122, 2267
Eke, V. R., Cole, S., Frenk, C. S., et al. 1996, MNRAS, 282, 263
Fukugita, M., Ichikawa, T., & Gunn, J. E. 1996, AJ, 111, 1748
Gilbank, D. G., Bower, R. G., Castander, F. J., & Ziegler, B. L. 2004, MNRAS, 348, 551
Gioia, I. M., Henry, J. P., Mullis, C. R., et al. 2001, ApJ, 553, 105
Girardi, M., Biviano, A., Giuricin, G., Mardirossian, F., & Mezetti, M. 1993, ApJ, 404, 38
Girardi, M., Giuricin, G., Mardirossian, F., Mezzetti, M., & Boschin, W. 1998, ApJ, 505, 74
Gladders, M. D., & Yee, H. K. C. 2000, AJ, 120, 2148
Goto, T., Sekiguchi, M., Nichol, R. C., et al. 2002, AJ, 123, 1807
Gunn, J. E., Hoessel, J. G., & Oke, J. B. 1986, ApJ, 306, 30
Gunn, J. E., Carr, M. A., Rockosi, C. M., et al. 1998, AJ, 116, 3040 (SDSS Camera)
Holden, B. P., Romer, A. K., Nichol, R. C., & Ulmer, M. P. 1997, AJ, 114, 1701
Hogg, D. W., Finkbeiner, D. P., Schlegel, D. J., & Gunn, J. E. 2001, AJ, 122, 2129
Horner, D. 2001, Ph.D. Thesis, University of Maryland
Katgert, P., Mazure, A., Perea, J., et al. 1996, A&A, 310, 8
Katgert, P., Biviano, A., & Mazure, A. 2004, ApJ, 600, 657
King, I. 1962, AJ, 67, 471
Ledlow, M. J., Voges, W., Owen, F. N., & Burns, J. O. 2003, AJ, 126, 2740
Lubin, L. M., Mulchaey, J. S., & Postman, M. 2004, ApJ, 601, 9
Lumsden, S. L., Collins, C. A., Nichol, R. C., et al. 1992, MNRAS, 258, 1
Lupton, R. H., Gunn, J. E., & Szalay, A. S. 1999, AJ, 118, 1406
Lupton, R., Gunn, J. E., Ivezić, Z., et al. 2001, in Astronomical Data Analysis Software and Systems X, ed. F. R. Harnden, Jr., F. A. Primini, & H. E. Payne (San Francisco: Astr. Soc. Pac.), ASP Conf. Ser., 238, 269 [arXiv:astro-ph/0101420]
Mazure, A., Katgert, P., den Hartog, R., et al. 1996, A&A, 310, 31
Merritt, D. R. 1987, ApJ, 313, 121
Mulchaey, J. S., Davis, D. S., Mushotzky, R. F., & Burstein, D. 2003, ApJS, 145, 39
Navarro, J. F., Frenk, C. S., & White, S. D. M. 1996, ApJ, 462, 563
Navarro, J. F., Frenk, C. S., & White, S. D. M. 1997, ApJ, 490, 493 (NFW)
Olsen, L. F., Scodeggio, M., da Costa, L., et al. 1999, A&A, 345, 681
Popesso, P., Böhringer, H., Brinkmann J., Voges, W., & York, D. G. 2004, A&A, 423, 449 (Paper I)

Popesso, P., Biviano, A., Böhringer, H., Romaniello, M., & Voges, W. 2005a, A&A, 433, 431 (Paper III)
Popesso, P., Böhringer, H., Romaniello, M., & Voges, W. 2005b, A&A, 433, 415 (Paper II)
Popesso, P., Biviano, A., Böhringer, H., & Romaniello, M. 2006, A&A, 445, 29 (Paper IV)
Postman, M. 1985, Huchra, J. P., Geller, M. J., & Henry, J. P. 1985, AJ, 90, 1400
Postman, M., Lubin, L. M., Gunn, J. E., et al. 1996, AJ, 111, 615
Retzlaff, J. 2001, XXIst Moriond Astrophysics Meeting, March 10−17, 2001 Savoie, France, ed. D. M. Neumann, & J. T. T. Van
Rosati, P., Borgani, S., & Norman, C. 2002, ARA&A, 40, 539
Scharf, C. A., Jones, L. R., Ebeling, H., et al. 1997, ApJ, 477, 79
Schechter, P. 1976, ApJ, 203, 297
Smith, J. A., Tucker, D. L., Kent, S. M., et al. 2002, AJ, 123, 2121
Stoughton, C., Lupton, R. H., Bernardi, M., et al. 2002, AJ, 123, 485
Strateva, I., Ivezić, Z., Knapp, G., et al. 2001, AJ, 122, 1861
Strauss, M. A., Weinberg, D. H., Lupton, R. H., et al. 2002, AJ, 124, 1810
The, L. S., & White, S. D. M. 1986, AJ, 92, 1248
Trümper, J. 1988, NATO Advanced Science Institutes (ASI) Series C, 249, 355
van der Marel, R. P., Magorrian, J., Carlberg, R. G., Yee, H. K. C., & Ellingson, E. 2000, AJ, 119, 2038
Voges, W., Aschenbach, B., Boller, T., et al. 1999, A&A, 349, 389
Wojtak, R., Łokas, E. L., Gottlöber, S., & Mamon, G. A. 2005, MNRAS, 361, L1
Yasuda, N., Fukugita, M., Narayanan, V. K., et al. 2001, AJ, 122, 1104
York, D. G., Adelman, J., Anderson, J. E., et al. 2000, AJ, 120, 1579
Zwicky, F., Herzog, E., Wild, P., Karpowicz, M., & Kowal, C. 1961−1968, Catalog of Galaxies and Clusters of Galaxies 1−6 (Pasadena: Caltech)

Online Material

Appendix A: The Abell Cluster Catalog

Table A.1. Here we list the properties of the 137 spectroscopically confirmed Abell systems extracted from the SDSS DR3, used in this paper. The meaning of the individual columns is the following: Col. 1: the name of the Abell cluster; Col. 2: the number of cluster members within 1 Abell radius; Col. 3: the cluster mean redshift; Col. 4: the cluster velocity dispersion and its error Col. 5: the cluster mass within r_{200}, M_{200}, in units of 10^{14} $M_{\odot}$; Col. 6: the cluster mass within r_{200} calculated using only the cluster red members, $M_{200,\rm red}$, in units of 10^{14} $M_{\odot}$; $M_{200,\rm red}$ is given only for the clusters with at least 10 red members; Col. 7: the fractional error on M_{200} and $M_{200,\rm red}$; Col. 8: the cluster virial radius, r_{200}, in Mpc; Col. 9: the cluster optical luminosity $L_{\rm op}$ and its error, in unit of 10^{12} $L_{\odot}$; Col. 10: the cluster X-ray luminosity in the ROSAT energy band (0.1−2.4 erg s^{-1}), in unit of 10^{44} erg s^{-1}; Col. 11: the fractional error on the X-ray luminosity; Col. 12: the Dressler & Shectman probability that a cluster does not contain substructures, $P_{\rm DS}$ (values <0.1 indicate clusters that are likely to contain substructures); Col. 13: the X-ray class: 0 for the normal X-ray emitting cluster, 1 for the Abell systems with less the 3σ X-ray detection, 2 for the X-ray non-detected Abell Clusters.

Name	$N_{\rm mem}$	$z_{\rm c}$	$\sigma_{\rm c}$	M_{200}	$M_{200,\rm red}$	er_M	r_{200}	$L_{\rm op}$	$L_{\rm X}$	$er_{L_{\rm X}}$	$P_{\rm DS}$	X-class
a0116	24	0.0661	582 ± 73	4.66	4.71	0.29	1.6	1.59 ± 0.35	0.090	0.25	0.19	0
a0117	95	0.0550	559 ± 41	4.03	3.85	0.15	1.5	2.52 ± 0.64	0.064	0.26	0.96	0
a0129	19	0.1501	749 ± 119	8.78	9.80	0.36	2.0	5.03 ± 1.87	0.548	0.26	0.62	0
a0130	21	0.1106	447 ± 84	2.81	2.34	0.37	1.4	2.12 ± 0.48	0.161	0.61	0.13	1
a0152	69	0.0589	729 ± 59	7.04	5.12	0.19	1.8	2.38 ± 0.52	0.057	0.25	0.09	0
a0168	110	0.0450	559 ± 36	3.57	2.89	0.14	1.5	2.70 ± 0.36	0.370	0.09	0.57	0
a0175	37	0.1285	606 ± 60	4.47	3.73	0.31	1.6	9.88 ± 2.53	1.114	0.29	0.84	0
a0190	17	0.1021	431 ± 122	2.19	0.61	0.66	1.2	1.64 ± 0.41	0.034	0.70	0.00	0
a0208	31	0.0793	499 ± 60	2.60	2.42	0.29	1.3	1.64 ± 0.32	0.237	0.22	0.68	0
a0243	32	0.1125	469 ± 50	2.52	2.04	0.30	1.3	2.83 ± 0.39	0.000	0.00	0.40	1
a0315	16	0.1740	636 ± 96	6.61	6.24	0.41	1.8	4.91 ± 0.91	0.056	1.20	0.50	2
a0351	14	0.1108	510 ± 118	2.70	2.27	0.42	1.3	2.35 ± 0.57	0.016	1.50	0.99	2
a0412	31	0.1092	585 ± 50	3.29	3.04	0.28	1.4	2.20 ± 0.69	0.071	0.53	0.11	2
a0441	25	0.1443	907 ± 554	17.17	4.80	1.25	2.5	5.95 ± 1.24	0.218	0.44	0.00	2
a0607	34	0.0962	501 ± 88	2.88	2.65	0.37	1.4	2.61 ± 0.42	0.023	0.57	0.56	1
a0620	14	0.1323	518 ± 76	2.17	2.78	0.61	1.2	3.34 ± 0.91	0.787	0.17	0.35	0
a0626	15	0.1168	757 ± 158	7.16	5.48	0.40	1.8	3.30 ± 0.83	0.092	0.44	0.32	0
a0628	61	0.0834	642 ± 63	5.98	4.46	0.19	1.7	2.81 ± 0.44	0.208	0.35	0.81	0
a0631	48	0.0826	577 ± 48	3.77	3.11	0.19	1.5	1.09 ± 0.27	0.061	0.42	0.49	0
a0646	29	0.1266	738 ± 96	10.45	9.72	0.24	2.1	3.82 ± 0.80	2.487	0.09	0.92	0
a0655	47	0.1276	736 ± 78	9.47	9.21	0.20	2.0	7.29 ± 0.94	2.527	0.16	0.88	0
a0660	26	0.0642	752 ± 138	7.91	7.61	0.43	1.9	1.62 ± 0.32	0.000	0.00	0.27	2
a0667	17	0.1441	512 ± 85	2.05	1.33	1.25	1.2	2.88 ± 0.63	1.998	0.11	0.53	0
a0682	17	0.1147	266 ± 242	0.75	0.22	2.12	0.9	1.07 ± 0.25	0.057	0.50	0.57	0
a0685	16	0.1464	496 ± 56	4.47	3.49	0.26	1.6	3.46 ± 0.88	0.000	0.00	0.07	2
a0714	29	0.1392	574 ± 78	4.97	4.86	0.26	1.6	4.16 ± 1.10	0.041	0.83	0.86	2
a0716	17	0.1188	494 ± 144	2.88	2.37	0.59	1.4	1.36 ± 0.43	0.009	1.50	0.46	2
a0729	28	0.0978	688 ± 87	3.38	3.90	0.36	1.4	1.21 ± 0.40	0.232	0.22	0.19	0
a0733	11	0.1156	392 ± 78	0.91	–	0.69	0.9	1.69 ± 0.51	0.535	0.62	0.49	0
a0736	42	0.0619	826 ± 98	10.11	9.08	0.29	2.1	4.66 ± 0.77	0.061	0.25	0.04	0
a0847	16	0.1508	704 ± 115	5.03	4.11	0.40	1.6	2.94 ± 0.54	0.730	0.21	0.87	0
a0856	19	0.1393	450 ± 69	1.92	2.61	0.48	1.2	1.74 ± 0.45	0.407	0.38	0.01	0
a0860	31	0.0965	941 ± 95	12.98	12.0	0.36	2.2	2.13 ± 0.46	0.313	0.23	0.00	0
a0861	17	0.1259	468 ± 104	3.29	2.88	0.44	1.4	2.51 ± 0.51	0.237	0.27	0.67	1
a0866	10	0.1435	266 ± 106	0.83	–	0.84	0.9	1.34 ± 0.39	0.143	0.47	0.12	1
a0869	12	0.1198	381 ± 127	1.74	2.02	0.66	1.2	1.81 ± 0.39	0.241	0.30	0.29	1
a0892	23	0.0943	470 ± 148	1.45	0.76	0.86	1.1	3.20 ± 1.56	0.175	0.26	0.09	0
a0912	28	0.0906	590 ± 82	3.72	3.05	0.31	1.5	3.01 ± 0.60	0.021	0.62	0.75	0
a0917	11	0.1370	403 ± 76	0.76	–	0.46	0.9	1.57 ± 0.37	0.252	0.31	0.24	1
a0919	12	0.0954	136 ± 37	0.21	–	0.66	0.6	0.59 ± 0.16	0.033	0.55	0.18	2
a0933	56	0.0965	455 ± 46	2.86	3.22	0.20	1.4	4.28 ± 0.89	0.387	0.21	0.87	0
a0975	14	0.1192	208 ± 58	0.48	–	0.50	0.8	0.67 ± 0.19	0.068	0.50	0.96	1
a1038	13	0.1275	253 ± 48	0.55	0.48	0.35	0.8	1.40 ± 0.27	0.108	0.44	0.83	0
a1064	17	0.1318	485 ± 93	2.30	2.21	0.34	1.3	2.39 ± 0.59	0.211	0.33	0.74	0
a1066	100	0.0690	731 ± 52	6.63	5.55	0.15	1.8	4.15 ± 0.60	0.657	0.17	0.35	0
a1072	11	0.1173	364 ± 83	1.45	–	0.67	1.1	1.12 ± 0.36	0.029	0.86	0.10	2
a1076	18	0.1168	418 ± 77	1.57	2.06	0.37	1.1	1.46 ± 0.30	0.295	0.21	0.96	0
a1078	11	0.1242	249 ± 51	0.50	–	0.66	0.8	1.38 ± 0.38	0.182	0.37	0.60	1
a1092	26	0.1058	449 ± 64	2.07	1.47	0.34	1.2	1.55 ± 0.35	0.000	0.00	0.02	2
a1107	15	0.1508	792 ± 104	10.03	10.3	0.33	2.1	2.61 ± 0.78	0.265	0.38	0.03	1
a1132	27	0.1358	880 ± 138	8.90	7.48	0.36	2.0	6.37 ± 0.95	3.038	0.07	0.45	0
a1139	89	0.0395	376 ± 34	1.68	1.07	0.19	1.2	1.16 ± 0.25	0.136	0.16	0.24	0
a1143	13	0.1379	459 ± 86	2.10	–	0.45	1.2	2.25 ± 0.56	0.030	0.80	0.10	2
a1164	19	0.1057	609 ± 144	4.24	5.79	0.54	1.6	1.75 ± 0.60	0.074	0.61	0.15	1
a1171	16	0.0577	161 ± 40	0.12	0.09	0.56	0.5	0.74 ± 0.17	0.024	0.55	0.01	1
a1189	37	0.0969	654 ± 196	4.58	4.26	0.59	1.6	2.63 ± 0.44	0.087	0.32	0.20	0

Table A.1. continued.

Name	$N_{\rm mem}$	$z_{\rm c}$	$\sigma_{\rm c}$	M_{200}	$M_{200,\rm red}$	er_M	r_{200}	$L_{\rm op}$	$L_{\rm X}$	$er_{L_{\rm X}}$	$P_{\rm DS}$	X-class
a1205	80	0.0761	865 ± 73	11.99	9.13	0.19	2.2	3.88 ± 0.54	0.976	0.09	0.01	0
a1218	23	0.0801	364 ± 75	0.91	0.63	0.39	0.9	0.81 ± 0.17	0.017	0.56	0.58	2
a1221	11	0.1103	289 ± 132	0.77	–	0.82	0.9	0.66 ± 0.32	0.000	0.00	0.66	2
a1236	38	0.1021	533 ± 59	3.72	2.27	0.29	1.5	2.57 ± 0.45	0.150	0.30	0.06	0
a1302	47	0.1153	691 ± 80	7.35	7.14	0.25	1.9	3.61 ± 1.08	1.307	0.09	0.72	0
a1346	74	0.0983	709 ± 54	7.64	4.59	0.18	1.9	3.98 ± 0.59	0.208	0.30	0.15	0
a1364	41	0.1066	553 ± 59	2.85	2.80	0.24	1.4	4.27 ± 0.94	0.040	0.80	0.55	2
a1366	42	0.1164	691 ± 70	7.72	8.13	0.20	1.9	2.61 ± 0.53	1.550	0.10	0.88	0
a1368	27	0.1293	735 ± 92	7.84	8.40	0.28	1.9	3.71 ± 0.65	0.130	0.47	0.06	0
a1376	16	0.1179	461 ± 204	3.11	3.43	0.88	1.4	1.62 ± 0.39	0.013	0.67	0.31	2
a1387	35	0.1310	692 ± 73	6.73	5.44	0.27	1.8	4.91 ± 0.66	0.693	0.20	0.05	0
a1392	11	0.1361	517 ± 146	3.86	–	0.61	1.5	3.11 ± 0.71	0.707	0.19	0.49	0
a1399	23	0.0910	251 ± 59	0.46	0.33	0.52	0.8	1.83 ± 0.27	0.000	0.00	0.03	2
a1406	14	0.1170	337 ± 97	1.48	0.96	0.59	1.1	1.85 ± 0.48	0.207	0.47	0.31	0
a1407	10	0.1349	561 ± 142	2.78	–	0.51	1.4	2.64 ± 0.50	0.423	0.28	0.78	0
a1411	10	0.1327	377 ± 98	1.41	–	0.92	1.1	1.54 ± 0.31	0.056	0.67	0.44	2
a1419	19	0.1077	504 ± 89	2.89	3.06	0.31	1.4	2.14 ± 0.50	0.233	0.30	0.96	0
a1424	83	0.0754	662 ± 45	5.49	4.88	0.14	1.7	2.32 ± 0.50	0.476	0.13	0.13	0
a1437	33	0.1341	1497 ± 13	39.89	30.5	0.17	3.2	7.27 ± 1.24	3.461	0.08	0.12	0
a1456	35	0.1346	540 ± 54	4.18	4.30	0.23	1.6	7.82 ± 1.72	0.431	0.27	0.63	1
a1457	17	0.0626	177 ± 42	0.29	0.27	0.61	0.6	0.40 ± 0.13	0.000	0.00	0.29	2
a1468	49	0.0869	361 ± 92	1.80	1.49	0.19	1.5	1.86 ± 0.94	0.004	1.00	0.33	2
a1496	56	0.0958	347 ± 46	1.53	1.29	0.30	1.1	1.85 ± 0.38	0.033	0.50	0.00	2
a1501	15	0.1336	406 ± 57	1.18	1.14	0.40	1.0	1.19 ± 0.32	0.268	0.26	0.61	0
a1507	65	0.0600	374 ± 42	1.36	0.92	0.23	1.1	1.47 ± 0.30	0.072	0.24	0.76	0
a1516	72	0.0765	705 ± 71	8.30	8.08	0.19	1.9	11.88 ± 3.12	0.151	0.27	0.65	0
a1518	23	0.1065	628 ± 118	4.49	2.40	0.41	1.6	2.61 ± 0.85	0.182	0.23	0.14	1
a1539	17	0.1072	510 ± 60	3.35	2.47	0.32	1.4	2.35 ± 0.61	0.043	0.55	0.30	2
a1559	45	0.1058	863 ± 124	14.06	11.5	0.33	2.3	3.61 ± 0.59	0.193	0.21	0.02	0
a1564	57	0.0790	633 ± 57	5.17	5.51	0.21	1.7	1.62 ± 0.40	0.072	0.29	0.11	1
a1566	28	0.1015	561 ± 69	3.52	4.04	0.24	1.5	1.65 ± 0.40	0.019	0.67	0.24	1
a1577	16	0.1388	359 ± 123	1.07	1.99	0.77	1.0	1.99 ± 0.34	0.095	1.14	0.72	2
a1579	15	0.1033	286 ± 86	1.00	1.15	0.73	1.0	0.46 ± 0.18	0.033	0.50	0.23	1
a1581	16	0.1503	521 ± 92	4.85	4.17	0.38	1.6	3.97 ± 0.61	0.103	0.46	0.22	2
a1599	30	0.0855	322 ± 38	0.84	0.58	0.40	0.9	10.98 ± 7.96	3.660	0.09	0.15	0
a1620	67	0.0846	782 ± 53	9.90	8.39	0.15	2.1	4.76 ± 0.94	0.002	4.00	0.04	0
a1621	32	0.1037	551 ± 61	2.12	2.24	0.31	1.2	10.03 ± 7.43	0.088	0.46	0.03	0
a1646	27	0.1055	573 ± 88	2.14	1.77	0.39	1.2	2.57 ± 0.86	0.219	0.23	0.71	0
a1650	70	0.0839	799 ± 87	11.14	9.51	0.22	2.1	4.00 ± 0.75	3.134	0.06	0.36	0
a1659	15	0.1067	383 ± 79	1.61	1.76	0.38	1.1	1.02 ± 0.21	0.028	0.62	0.80	2
a1663	86	0.0830	703 ± 60	7.62	7.57	0.17	1.9	3.01 ± 0.52	0.548	0.15	0.22	0
a1674	17	0.1051	549 ± 98	4.05	4.15	0.46	1.5	2.24 ± 0.41	0.172	0.26	0.46	0
a1678	16	0.1689	390 ± 124	1.98	1.64	0.67	1.2	1.90 ± 0.50	0.143	0.50	0.14	1
a1692	54	0.0845	561 ± 65	4.69	3.75	0.24	1.6	2.00 ± 0.42	0.090	0.35	0.56	0
a1701	21	0.1239	413 ± 54	1.15	1.0	0.49	1.0	1.76 ± 0.45	0.138	0.86	0.49	1
a1750	115	0.0858	784 ± 41	10.27	9.43	0.12	2.1	12.05 ± 2.00	1.770	0.10	0.00	0
a1767	127	0.0705	884 ± 55	11.57	8.68	0.14	2.2	3.59 ± 0.64	1.329	0.05	0.17	0
a1773	82	0.0773	779 ± 74	9.07	6.43	0.17	2.0	4.57 ± 0.66	0.753	0.13	0.71	0
a1780	55	0.0776	450 ± 46	2.51	2.72	0.22	1.3	2.55 ± 0.36	0.033	0.61	0.17	1
a1809	99	0.0795	716 ± 52	5.83	5.05	0.16	1.7	5.30 ± 1.13	1.002	0.09	0.85	0
a1872	12	0.1480	694 ± 138	3.89	–	0.43	1.5	1.95 ± 0.47	0.253	0.30	0.05	0
a1882	55	0.1396	733 ± 99	7.44	6.25	0.26	1.9	13.29 ± 1.42	0.192	0.39	0.19	0
a1918	20	0.1402	935 ± 129	16.26	12.3	0.30	2.4	5.73 ± 1.68	2.448	0.08	0.60	0
a1937	13	0.1380	223 ± 50	0.23	0.21	0.62	0.6	1.02 ± 0.29	0.239	0.47	0.32	0
a1938	18	0.1376	601 ± 70	4.95	5.78	0.26	1.6	8.82 ± 3.74	0.714	0.22	0.52	0
a2026	51	0.0908	753 ± 59	6.73	5.43	0.19	1.8	4.44 ± 1.20	0.141	0.31	0.80	0
a2030	51	0.0915	460 ± 54	2.27	1.80	0.25	1.3	2.50 ± 0.40	0.081	0.35	0.79	0
a2050	34	0.1193	826 ± 165	10.84	7.89	0.36	2.1	4.85 ± 0.87	1.505	0.14	0.26	0
a2082	31	0.0862	380 ± 111	1.84	1.42	0.56	1.2	1.99 ± 0.33	0.065	0.38	0.56	0
a2094	36	0.1446	606 ± 110	4.41	3.01	0.35	1.6	5.18 ± 0.65	0.815	0.24	0.90	0
a2118	24	0.1416	572 ± 91	4.41	3.34	0.32	1.6	3.39 ± 0.91	0.158	0.37	0.32	1
a2149	60	0.0650	330 ± 46	1.49	1.09	0.28	1.1	2.13 ± 0.33	0.400	0.08	0.87	0
a2196	19	0.1340	422 ± 131	2.17	2.71	0.58	1.2	2.72 ± 0.45	0.492	0.17	0.80	0
a2211	15	0.1361	493 ± 100	2.71	3.32	0.38	1.4	0.81 ± 0.32	0.050	0.50	0.92	1
a2235	15	0.1492	855 ± 195	12.24	12.2	0.47	2.2	6.26 ± 0.96	1.176	0.14	0.91	0
a2243	36	0.1067	759 ± 85	6.37	6.62	0.29	1.8	2.13 ± 0.38	0.357	0.15	0.18	0
a2244	83	0.0993	1062 ± 61	14.89	11.7	0.13	2.3	6.84 ± 0.71	4.005	0.04	0.05	0

Table A.1. continued.

Name	$N_{\rm mem}$	$z_{\rm c}$	$\sigma_{\rm c}$	M_{200}	$M_{200,\rm red}$	er_M	r_{200}	$L_{\rm op}$	$L_{\rm X}$	$er_{L_{\rm X}}$	$P_{\rm DS}$	X-class
a2255	176	0.0801	1121 ± 67	19.56	16.7	0.12	2.6	11.14 ± 2.83	2.443	0.02	0.54	0
a2259	16	0.1600	1080 ± 15	18.15	19.2	0.30	2.5	11.32 ± 1.78	2.913	0.09	0.01	0
a2356	23	0.1195	716 ± 85	5.84	5.45	0.25	1.7	3.30 ± 0.59	0.670	0.18	0.31	0
a2379	14	0.1234	531 ± 105	3.23	–	0.39	1.4	3.29 ± 1.24	0.027	1.40	0.44	2
a2399	111	0.0579	569 ± 37	4.09	3.19	0.14	1.5	3.54 ± 0.43	0.490	0.12	0.07	0
a2428	42	0.0839	420 ± 23	2.17	2.12	0.15	1.2	2.57 ± 0.67	1.351	0.14	0.84	0
a2433	16	0.1195	257 ± 44	0.50	0.33	0.40	0.8	0.84 ± 0.22	0.092	0.47	0.66	0
a2448	38	0.0820	447 ± 62	2.56	2.14	0.28	1.3	2.05 ± 0.49	0.029	0.54	0.64	2
a2505	21	0.1100	366 ± 57	0.94	1.01	0.40	1.0	1.58 ± 0.29	0.238	0.28	0.00	0
a2561	13	0.1634	405 ± 91	1.17	1.23	0.50	1.0	2.16 ± 0.38	1.720	0.25	0.72	1
a2564	20	0.0828	339 ± 70	1.25	1.40	0.45	1.0	0.93 ± 0.20	0.041	0.38	0.45	0
a2593	167	0.0419	570 ± 55	4.53	3.68	0.18	1.6	3.24 ± 0.53	0.485	0.07	0.74	0
a2670	109	0.0761	804 ± 51	9.40	9.32	0.13	2.0	5.08 ± 0.56	1.255	0.10	0.73	0
a2705	33	0.1165	452 ± 64	3.45	3.65	0.30	1.5	3.77 ± 0.58	0.018	0.50	0.03	1